# Design exploration of UAM vehicles

Wang, Sen; Pereira, Lourenço Tércio Lima; Ragni, Daniele

**DOI**
10.1016/j.ast.2025.110058

**Publication date**
2025

**Document Version**
Final published version

**Published in**
Aerospace Science and Technology

Aerospace Science and Technology 160 (2025) 110058

Contents lists available at ScienceDirect

Aerospace Science and Technology

journal homepage: www.elsevier.com/locate/aescte

# Design exploration of UAM vehicles

Sen Wang [*], Lourenço Tércio Lima Pereira [*], Daniele Ragni

*Flow Physics and Technology Department, Delft University of Technology, Kluyverweg 1, Delft, 2629HS, South Holland, the Netherlands*

ARTICLE INFO

Communicated by George N. Barokas

*Keywords:*
Urban air mobility design exploration
Urban air mobility noise emissions

ABSTRACT

This study describes a design exploration of Urban Air Mobility (UAM) vehicles, based on top-level aircraft requirements. The exploration focuses on a fully electric vertical takeoff and landing (eVTOL) vehicle that employs an architecture of conventional airframe coupled with tilted rotors, aimed to carry four passengers. Using a low-fidelity design framework, a variety of configurations are investigated by altering design variables such as wing area, number of propellers, operating speed, and range. The influence of these variables on the design is explored from the environmental, societal and, economical perspectives for a 2050 time horizon. The findings suggest that configurations with a small wing area and a large number of small propellers emerges as preferable for minimizing energy consumption (per pax-km) and operating expenses (per pax-km). However, in terms of noise emissions, configurations with fewer but larger propellers are favoured, marking a departure from the design choices that prioritize energy efficiency and cost. Additionally, the study underscores that operations prioritizing commercial viability require high-speed cruising and reduced flight hours, diverging from those that prioritize energy efficiency, thereby emphasizing the necessity of multidisciplinary optimization. Finally, a noise-estimation model is developed to enable quick assessment of the vehicle's sound power level. The model necessitates only fundamental powertrain information as inputs and provides insights into the impact of design choices on noise emission, which is beneficial at preliminary design stage.

## 1. Introduction

Urban air mobility (UAM) is defined as an on-demand aviation service, projected to become viable in the near-future market [1]. As an integral part of the Advanced Air Mobility (AAM) initiative, UAM aims to fill the voids left by conventional aviation industries [2] through the use of novel Vertical TakeOff and Landing (VTOL) vehicles. The concept focuses on facilitating flight operations within and around urban areas, primarily for the passengers' and cargo mobility. In recent years, a growing interest in UAM is observed, driven by technological developments in electric propulsion, electronic control systems, and energy storage. This increasing focus has accelerated the development of electric VTOL (eVTOL) vehicles, leveraging the advantages of design versatility, control authority, and lower noise and gas emissions. Of important aspects, studies have focused on relevant perspectives of UAM application, including its safety, community acceptance, and economic feasibility [3,4].

The adoption of electric powered eVTOL vehicles faces significant challenges due to the current state of battery technologies [5]. This issue arises from the currently low energy density of lithium-ion batteries, which is limited around 230-250 Wh/kg on cell level [6]. Hence, achieving desired operating ranges may lead to an excessively heavy takeoff mass. Given this limitation, much of UAM developments focus on urban operations, with intercity and regional operations receiving comparatively less attention [7]. However, anticipated advancements in the fields of batteries [8,9], electric motors [10], combined with hydrogen fuel cells [11] are expected to make long-distance operation more feasible.

To mitigate the limitation of energy storage, attention is given to the appropriate eVTOL architecture and sizing to minimize the energy consumption in operation. Three architectures are notably explored, i.e. multirotors, lift-and-cruise, and tilted rotors. While the first architecture uses rotors as sources of lift during the entire vehicle mission, the latter two take advantage of fixed wing-based lift to reduce power consumption during cruise. Comparative analyses of eVTOL architectures indicate that a conventional airframe coupled with tilted rotors provides enhanced flexibility in improving vehicle performance for different operating ranges [12]. The high-power demand in this configuration is

* Corresponding authors.
*E-mail addresses:* S.Wang-2@tudelft.nl (S. Wang), l.t.limapereira@tudelft.nl (L.T. Lima Pereira), d.ragni@tudelft.nl (D. Ragni).

https://doi.org/10.1016/j.ast.2025.110058
Received 16 August 2024; Received in revised form 29 January 2025; Accepted 11 February 2025
Available online 13 February 2025

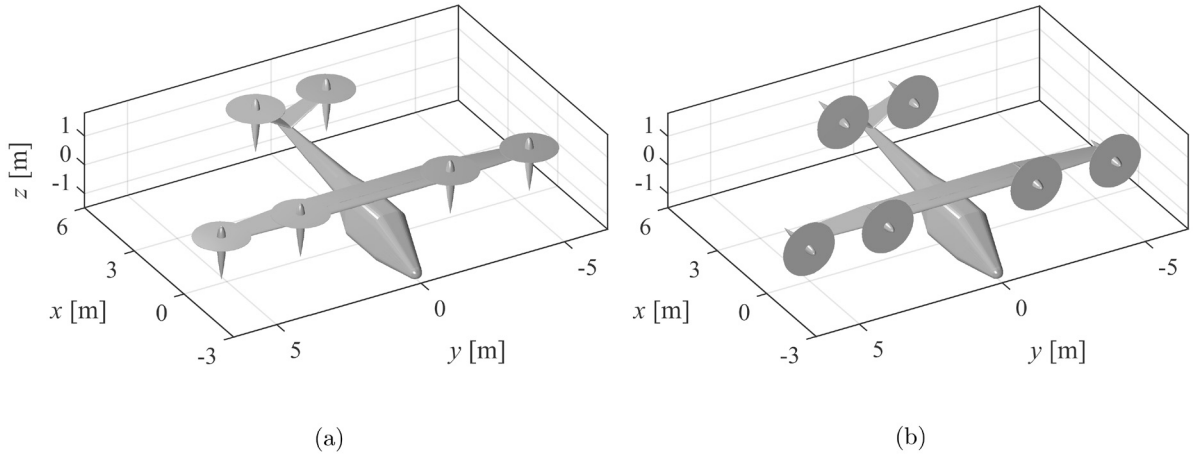


**Fig. 1.** A sample of vehicle design in (*a*) VTOL and (*b*) cruise configurations.

restricted primarily to mission phases such as takeoff/landing, climb/descent, and hovering. This approach effectively reduces energy consumption during the cruise phase, thereby decreasing the necessary battery weight. Furthermore, it offers more space for optimizing propeller design, as tiltable rotors can be fully utilized across all mission phases, e.g., takeoff and cruise [12]. These advantages, however, come with certain drawbacks. For instance, fixed wings add to the total weight of the vehicle. Additionally, the rotor-tilting mechanism introduces technical complexity and safety concerns, and it can also lead to an increase in the size and weight of the powertrain [12].

In addition to the technological challenges, social acceptance is another crucial factor for UAM operations. A recent study conducted for EASA [13] indicates that the feasibility of UAM operations is closely associated with the noise emission of UAM vehicle, as noise annoyance from UAM is a major concern among EU citizens. According to FAA regulation (14 CFR 36.1103), tilt-rotor vehicles weighting between 1000 kg to 3000 kg, which are typical for UAM operations, have limits on effective perceived noise level (EPNL) between 90 EPNdB and 95 EPNdB for takeoff, approach, and flyover at around 150 m above ground. Similar regulations have also been proposed by EASA, following the noise standards defined by ICAO (Annex 16 Vol. 1). Historic instances show that failing to comply with the noise regulations can lead to strict noise ordinances [14,15], affecting the installation of vertiports, restricting the flight routes and operational frequency.

A brief survey on UAM design exploration reveals that few studies have conducted comprehensive investigations to systematically address the relationship between the design rationale of UAM vehicles and constraints from environmental, societal, and economical perspectives. In light of that, exploring the relevant design variables is crucial to identify the optimum configurations that can fulfil the given mission objectives while having minimal impact on the surrounding environment and remaining economically competitive. To address the associated design concerns, a preliminary design exploration was conducted in this study. This exploration follows the framework of the COLOSSUS (Collaborative System of Systems Exploration of Aviation Products, Services, and Business Models) project [16] (Horizon Europe framework programme), which employs a holistic approach to tackle challenges by developing a system-of-systems (SoS) design methodology that combines the optimization of aircraft, operations, and business models [17].

In this investigation, the preliminary design of the UAM vehicles was performed using a low-fidelity design framework developed at Delft University of Technology. The conceptual designs feature an architecture of conventional airframe coupled with tilted rotors. A set of design choices that influence the performance of UAM vehicle are considered in the exploration. These design choices are the operating range, cruise speed, number of propellers, and wing area. The assessment of the influence of these design variables is conducted by means of energy consumption, noise emission, and commercial viability. The study is based on a scenario where the entry in service (EIS) is set for 2050, following the significant development of the market [18] and technologies [8–10]. Optimum configurations for each criterion are identified, and the results provide direct choice guidelines in response to the specified constraints. Additionally, based on the results of this design exploration, a noise estimation model is developed to enable quick estimation of the emitted sound power level (PWL) during takeoff and cruise. The model requires only basic powertrain information and provides insights for design choices aimed at reducing noise emissions, making it ideal for the preliminary design stage.

## 2. Methodology

The design exploration was carried out using a low-fidelity multidisciplinary design framework [19] developed at Delft University of Technology. The framework is based on analytical and semi-empirical methods, intending to facilitate a preliminary design process of eVTOL vehicles using a set of feasible Top-Level Aircraft Requirements (TLARs) to drive the design activities. These TLARs are derived from the assessment of operating scenarios and existing prototypes [20]. In this section, the design process workflow is briefly introduced along with the assumptions given to the design.

### 2.1. Vehicle architecture and mission definition

The design framework [19] is based on a tilted rotor configuration with fixed landing gear, V-tail stabilizers, two propellers mounted on the tip of the tails and the others evenly distributed over the wing. Fig. 1 (a) and (b) demonstrate a sample vehicle configuration during takeoff and cruise, respectively. The chosen architecture is based on the existing Joby S4 vehicle, for which a considerable amount of data is publicly available, and has been demonstrated as a feasible design with test flights [21]. Following our previous work [19], the design framework was validated by aligning its input variables with those of a reference vehicle and comparing the resulting system-level vehicle attributes. Table 1, adapted from [19], presents a comparison of design variables and system-level vehicle characteristics between the framework's predictions and those of the Joby S4 production prototype. A pack-level energy density of 235 Wh/kg was adopted, consistent with the Joby S4 specifications. The results show a reasonable agreement between the predicted and reference values, validating the design framework for preliminary design purposes. It should be noted that the comparison is based on publicly available data (Vertical Flight Society), and actual figures may differ from those reported. For readers' interest, additional exploration of UAM from a SoS perspective can be found in the work

**Table 1**
Adapted comparison of design variables and vehicle characteristics between design framework and Joby S4 (production prototype) [19].

| | unit | Design framework | Joby S4 |
|---|---|---|---|
| Number of pilots | - | 1 | 1 |
| Number of passengers | - | 4 | 4 |
| Number of propellers ($N_{prop}$) | - | 6 | 6 |
| Wing span ($b$) | [m] | 10.7 | 10.7 |
| Energy density (pack level) | [Wh/kg] | 235 | 235 |
| Operating range ($R$) | [km] | 161 | 161 |
| Cruise speed ($V$) | [km/h] | 322 | 322 |
| Empty mass | [kg] | 2,193 | 1,950 |
| Maximum takeoff mass (MTOM) | [kg] | 2,768 | 2,404 |
| Total power | [kW] | 1,162 | 1,416 |
| Wing loading | [kg/m$^2$] | 194 | 171 |
| Power loading | [kg/kW] | 2.4 | 1.7 |

**Table 2**
Mission definitions across various stages.

| | Duration | Speed | Distance | Load factor | Pct |
|---|---|---|---|---|---|
| unit | [s] | [m/s] | [km] | - | [%] |
| Takeoff | 10 | 0 | - | 1.0 | 67 |
| Climb | - | 2.5 | 0.3 | 1.1 | 60 |
| Cruise | - | $V$ | $R$ | 1.0 | 40 |
| Loiter | 1,200 | $V$ | - | 1.0 | 44 |
| Descent | - | 2.5 | 0.3 | 1.0 | 30 |
| Landing | 10 | 0 | - | 1.0 | 67 |

of Prakasha et al. [22], which examines various aircraft architectures, fleet combinations, technology scenarios, and operational strategies.

In this study, the mission performed by the vehicle consists of 6 stages, takeoff, climb, cruise, loiter, descent, and landing. Fast takeoff and landing are assumed for operation in urban areas, while the vehicle sustains unity load factor. The vehicle climbs and descends at a rate of 2.5 km/h. The vehicle load factor is considered 1.1 for the climb and unity for descent. Cruise takes place at a defined altitude of 300 m, with the range and speed specified during the design exploration. Additionally, the design accounts for a 20-minute loiter time to fulfil the fuel requirements for operating rotorcrafts in VFR (Visual Flight Rules) condition, as mandated by the FAA (14 CFR 91.151). To reduce energy consumption, the loiter stage is assumed as the vehicle maintaining its altitude while circling around the vertiport at cruise speed. Table 2 describes the considered mission stages, and the corresponding initial guess on the percentage power (Pct) with respect to the total installed power.

### 2.2. Preliminary design framework

The design process begins by defining the aforementioned TLARs. Using these inputs, a propulsion system is sized to meet the required operating conditions using actuator disk theory [23]. Subsequently, a first-order mass estimation of the vehicle is carried out through Roskam method [24], where the relation between empty weight and Maximum TakeOff Mass (MTOM) is taken from [25]. The sizing process on the propulsion system and first-order mass estimation iterates until convergence is reached for the Maximum TakeOff Mass (MTOM) and total installed power. As universally accepted sizing formulas for eVTOL aircraft have not yet been established, the current design framework mainly adopts the Cessna method, which is conventionally used for sizing small, lightweight, and low-performance aircrafts due to its alignment with the characteristics of UAM vehicles [24]. Note the method is mainly driven by the geometric dimension of the aircraft and mission profile.

In parallel to the aforementioned sizing process, the aerodynamic characteristics of the vehicle, e.g., coefficient of lift and drag etc., are estimated based on the viscous solution of XFOIL [26] and lifting-line theory [27]. The initial configuration of the UAM-model geometry that meets the revised mission requirements (derived from the first iterative sizing process) is created from the analysed parameters.

Following the aerodynamic characteristics of the vehicle, the design enters another iterative process that encompasses the aerodynamic performance evaluation and second-order mass estimation [24]. At this stage, mass estimation at system levels is progressively refined, and the corresponding aerodynamic performance is continuously updated and revised. The process converges when the determined cruise range meets the mission requirement. Here, the battery sizing is the main process that influences the loop. It is important to highlight that, during this step, the vectored thrust can also be employed to ensure level flight in all conditions in case the wing-based lift is insufficient. The approach permits the exploration of design choices in which the rotors also contribute to lift, giving insights into the performance trends shifting from multicopter- to tilt-rotor-like.

After these design iterations, the acoustic noise generated by operating UAM vehicle is evaluated. Based on the specifications of the propulsion system and the revised mission profile, the tonal and broadband noise components of an isolated propeller are assessed through Hanson's model [28] and Schlinker and Amiet model [29], respectively. Noise estimations are conducted by considering the actuator disk as a point source rotating at a radius equal to 70% of the propeller radius. The overall noise of multi-propeller configuration is obtained by superimposing the results of each isolated propeller. Note that the evaluation does not take into account the aerodynamic interference between propellers, fuselage, wing, and the acoustic constructive and destructive interference. In addition, several studies have demonstrated the importance of propeller integration in noise estimation [30,31], while the computed results do not account for unsteady interactions, which emit more strongly in the axial direction of the rotor [32]. Following the work of Fuerkaiti et al. [33], the emissions are computed over an imaginary sphere covering the vehicle. The sphere is then treated as a noise source, which allows for the prediction of the ground-level noise signature. The results shown here will only focus on the A-weighted sound power level produced by the vehicles.

### 2.3. Design of experiments

In the context of this study, the TLARs are closely aligned with the mission definition and vehicle layout, encompassing operating range $R$, cruise speed $V$, number of propellers $N_{prop}$, and wing area $S$. The range of $R$ is draw from the market analysis conducted by NASA [34], and is set between 25 km to 300 km for both UAM and Regional Air Mobility (RAM) operations. A set of $V$ is also considered since $V$ governs the mission duration and operating expenses [34], and is linked to the competitiveness of the UAM vehicle compared to other means of transpositions. In reference to existing prototypes [12], the range of $V$ is selected as 100 km/h to 325 km/h. As previously mentioned, the conceptual design features fixed wings and tilted rotors, different number of propellers ($N_{prop}$) and wing area ($S$) are therefore considered to facilitate a variety of configurations. The corresponding values of aforementioned TLARs are summarized in Table 5, and a total of 2,400 vehicle configurations are assessed. It's important to note that the modification of $S$ is achieved by adjusting the wing aspect ratio (AR) while keeping the wing span constant, i.e., linearly reducing AR leads to a non-linear increase in $S$. The approach enables the assessment of vehicle aerodynamic performance without excessively increasing its ground footprint, taking into account that the operations will be conducted in urban areas. In reference to the design of Joby S4, which has a similar mission profile and architecture, this top-level assessment assumes a series of other design parameters including wing span ($b$ = 10.7 m), fuselage length ($l_{fus}$ = 8 m), number of pilot ($N_{pilot}$ = 1), and number of passengers ($N_{pax}$ = 4). The fuselage is 1.5 m tall ($H$) with a height-to-width (HW) ratio of 1.5. Its nose section is approximately 2.3 m long ($l_{nose}$) and has a windshield angle $\psi$ of 35°. The fuselage tail angle $\phi$ is set to 40°, and the tail boom sweeps up at $\theta$ = 4°over a length of 4 m ($l_{tail}$). The dimension of the

**Table 3**
Summary of geometric and dimensional assumptions of the vehicle.

| | $b$ | $l_{fus}$ | $l_{nose}$ | $l_{tail}$ | HW | $\psi$ | $\phi$ | $\theta$ | $V_h$ | $V_v$ |
|---|---|---|---|---|---|---|---|---|---|---|
| unit | [m] | [m] | [m] | [m] | - | [°] | [°] | [°] | - | - |
| Value | 10.7 | 8 | 2.3 | 4 | 1.5 | 35 | 40 | 4 | 0.7 | 0.04 |

**Table 4**
Summary of assumptions on the propulsion system.

| | ED | PD | $\eta_m$ | $r_{PW}$ | $B$ | $s$ | $C_L$ |
|---|---|---|---|---|---|---|---|
| unit | [Wh/kg] | [kW/kg] | [%] | [kW/kg] | - | - | - |
| Value | 585 | 11.3 | 97 | 0.4 | 5 | 0.25 | 1.5 |

**Table 5**
Summary of TLARs assessed for the design of experiments.

| | $R$ | $V$ | $N_{prop}$ | $S$ | AR |
|---|---|---|---|---|---|
| unit | [km] | [km/h] | - | [$m^2$] | - |
| Increment | 25 | 25 | 2 | - | 1 |
| Range | 25 - 300 | 100 - 325 | 4 - 10 | 11 - 19 | 6 - 10 |

V-tail is estimated using the conventional horizontal and vertical tails with volume coefficients of $V_h = 0.7$ and $V_v = 0.04$, respectively [35]. Table 3 presents a summary of the vehicle's geometric and dimensional assumptions.

In this exploration, an EIS time of 2050 is considered, by which up to 5.5 million UAM vehicles are expected to operate at peak hours globally [18], and solid-state battery technology is widely adopted. The EIS time is proposed within the framework of the project COLOSSUS [16]. Corresponding assumptions are made based on technological projections of battery [8,9] and electric motors [10]. The battery is expected to have a pack-level energy density (ED) of 585 Wh/kg with a nominal c-rate of 4/h. This rather optimistic ED is assumed to reduce constraints imposed by battery technology. The electric motor's power density (PD) and mean efficiency ($\eta_m$) are anticipated to be 11.3 kW/kg and 97%, respectively. Propeller efficiency and figure of merit are computed based on the number of blades ($B$) and propeller solidity factor ($s$), according to [36]. Referencing the Joby S4, the blade number is set to 5 and a constant solidity of 0.25 is assumed in this study. To initiate the powertrain sizing, an initial power-to-weight ratio ($r_{PW}$) value of 0.4 kW/kg is considered, which is comparable to those observed in VA-X4 (0.42 kW/kg) and Joby S4 (0.59 kW/kg). The propellers are expected to have pitch control, and the section lift coefficient ($C_L$) of blade is assumed to be 1.5 (Clark Y airfoil) for optimal thrust production. The aforementioned assumptions on the design of propulsion system are summarized in Table 4.

To streamline the design process, several design filters are employed to identify the optimal configurations within the scope of this design exploration. These filters are chosen based on criteria of energy consumption (EC), noise emission, and commercial viability. The first filter EC is defined by the sum of energy consumed by the vehicle across all stages of mission. The second filter focuses on a single-value evaluator, specifically the sound power level of (PWL) of vehicle during both takeoff and cruise stages. Note the PWL values are computed using A-weighted SPL to account for the human-ear sensitivity over frequency spectrum [37]. Furthermore, a design filter based on operating expenses (OE) is employed to identify the ideal configurations from the commercial perspective. Following Brown and Harris [38], OE is computed from direct operating cost (DOC) and indirect operating cost (IOC), while the former cost can be further divided into pilot cost, maintenance cost, and energy cost. The pilot cost and maintenance cost are estimated using an average wrap rate around €100/h and €60/h, respectively [38]. Note the maintenance time is considered around 62.5% per flight hours [38]. Using a conservative approach, the flight hours and maintenance time are rounded up to the nearest integer when computing OE. The operating cost also depends on the size of the aircrew, while the number of pilots is fixed to one here. The energy cost is approximated based on the average non-household electricity price (first half of 2023, European Commission), which is €0.1833 $kWh^{-1}$. The value of IOC is then approximated from 40% of DOC [38]. The projection of electricity price for 2050 is not considered here.

## 3. Results and discussions

In this section, assessments on eVTOL design exploration are carried out, focusing on a set of design variables: $S$, $N_{prop}$, $V$, and $R$. The discussion is organized into four parts. The first part investigates the influence of design variables associated with the vehicle configuration, namely $S$, and $N_{prop}$, offering some insights into the design rationale. The second part focuses on exploring the optimal performance scenarios, which are characterized by $V$ and $R$. Numerous design filters are employed to identify the ideal configuration under various operating conditions. Subsequently, the configurations deemed commercially viable are reported, and the relation between the aforementioned variables is discussed. In the end, a regression model is proposed to assess noise emissions based on the results of this exploration. The model utilizes basic powertrain information and elucidates the impact of design choices on noise emissions. Within the section, the subscripts 'p' and 'pk' indicate that the variable is normalized per passenger and per passenger-kilometer, respectively. The former normalization is utilized to analyze the overall variations per flight, while the latter allows for interpreting the results despite differences in operating range, offering guidance suitable for different business models. All the equations and values reported in this study are in SI units, unless otherwise specified. For interpretation of the colours in the following content, the reader is referred to the web version of this article.

### 3.1. Aircraft design considerations

Aircraft sizing considerations, i.e. $S$ and $N_{prop}$, are first investigated to unveil their influence on energy consumption (EC), noise levels, and commercial viability. Assessments are performed using design filters of energy consumption in kWh/pax/km ($EC_{pk}$), A-weighted sound power level during takeoff ($PWL_t$) and cruise ($PWL_c$), and operating expenses in €/pax/km ($OE_{pk}$).

The evaluation of $S$ and $N_{prop}$ through $EC_{pk}$ is conducted over a range of $V$ and $R$, which leads to a total of 2,400 vehicle configurations. Representative results (500 configurations) are demonstrated in Fig. 2, which consists of 25 contour plots, each corresponding to a specific operating condition determined by $R$ (in columns) and $V$ (in rows). The values of $R$ and $V$ are annotated on the top and right sides of the figure, respectively. Within each contour, the variation of $EC_{pk}$ is illustrated with respect to $S$ and $N_{prop}$. The local minimum of each contour is highlighted using a red-bordered box to facilitate the assessment of design preferences across operating scenarios. The evaluation of $EC_{pk}$ shows that $EC_{pk}$ span over a wide range between approximately 0.1 kWh/pax/km and 60 kWh/pax/km. The level of $EC_{pk}$ is significantly higher at $V = 100$ km/h than at other speeds. In Fig. 2, the presented upper limit of $EC_{pk}$ is capped at 1 kWh/pax/km to help visualize the variation in $EC_{pk}$ at other speeds. The lowest level of $EC_{pk}$ is observed to occupy a notable region in the contours associated with $V = 150$ km/h and is still present at $V = 200$ km/h, though in a smaller area. Further increasing $V$ diminishes the presence of minimum $EC_{pk}$. The significant difference between the overall level of $EC_{pk}$ at speed of 100 km/h and higher is attributed to a change in the vehicle's lifting characteristics with increasing $V$. At $V = 100$ km/h, the vehicle relies heavily on propellers to maintain altitude during cruise, thereby functioning similarly to a multicopter. The observation suggests that the tilt-rotor architecture requires a minimum operating speed to effectively utilize the installed wings. This speed is found to be between 125 km/h and

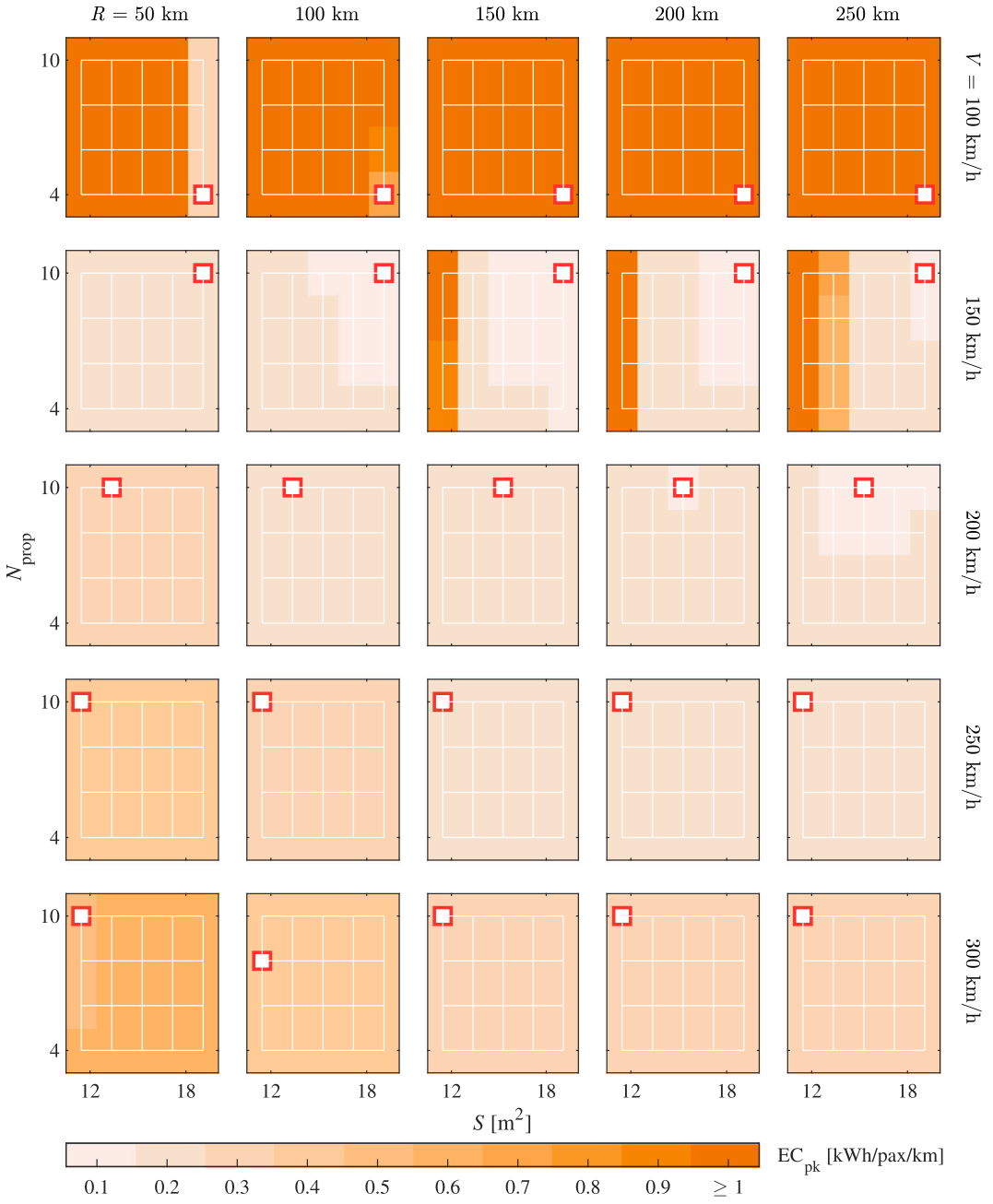


**Fig. 2.** Contours of the energy consumption in kWh/pax/km ($EC_{pk}$) with varying $N_{prop}$ and $S$, across different operating scenarios defined by $V$ and $R$. The configuration corresponding to local minimum (within the contour) is highlighted by red-bordered box. (For interpretation of the colours in the figure(s), the reader is referred to the web version of this article.)

175 km/h, depending on $R$. It's also worth noting that further increasing $S$ is unrealistic, as the corresponding AR (approaching 4) would be similar to those of delta wings.

Regarding the influence of $N_{prop}$, the result reveals that $EC_{pk}$ is proportional to $N_{prop}$ at $V = 100$ km/h, and $N_{prop} = 4$ appears to be the preferable design choice in this case. The relation between $N_{prop}$ and $EC_{pk}$ can be explained by inspecting the size of the actuator disk. First of all, the design exploration shows an inverse relation between total actuator disk area and $N_{prop}$, as it is confirmed that individual actuator disk area $A_D$ is proportional to the cube of thrust per propeller $T$ during takeoff as shown in Equation (1) [23,39],

$$A_D = \frac{T^3}{2\rho P^2}, \tag{1}$$

where $\rho$ represents the density of air and $P$ corresponds to the takeoff power per propeller. Both $P$ and $T$ are associated with the maximum takeoff mass (MTOM) of the vehicle and can be expressed in the form of

$$P = k\frac{\eta_p r_{PW} \mathrm{MTOM}}{N_{prop}}, \text{and} \tag{2}$$

$$T = g\frac{r_{TW} \mathrm{MTOM}}{N_{prop}}, \tag{3}$$

where $g$ is the gravitational constant. Here, $r_{PW}$ and $r_{TW}$ denote the assumed power-to-weight and thrust-to-weight ratios, respectively, which are integral to the powertrain sizing process. As discussed in Section 2.3, an initial conservative $r_{PW}$ of 0.4 kW/kg is adopted and will be refined throughout the design process. The powertrain efficiency $\eta_p$ is assumed

to be 0.87. The value of $k$ is set below one, indicating that a fraction of installed power is utilized for takeoff. The value of $r_{TW}$ is defined as $N_{prop}/(N_{prop}-2)$, which yields a ratio of 2:1 for configurations with 4 propellers to ensure aviation safety during takeoff. This ratio decreases as $N_{prop}$ increases, reflecting the reduced impact of each individual propeller on overall aviation safety. For a given MTOM, a larger $N_{prop}$ results in a smaller $r_{TW}$, leading to smaller $T$ and $A_D$. It is also interesting to note that this relation satisfies the space constraint on propeller installation, as the propeller diameter is inversely proportional to $N_{prop}$ when they are distributed over wing.

Next, evaluating the relation between $P$, $T$, and $A_D$ during cruise is essential for elucidating the inverse relation between $N_{prop}$ and $EC_{pk}$. This is attributed to the fact that the energy spent during cruise constitutes the overall energy consumption. According to the work of Van Kuik [39], the relation between $P$ and $A_d$ during cruise is characterized by the following equation

$$\frac{P}{\rho V^3 A_D} = 2\left(\frac{\langle V_d\rangle}{V}\right)^2\left(\frac{\langle V_d\rangle}{V}-1\right), \tag{4}$$

where $\langle V_d\rangle$ is the average velocity over actuator disk, and can be obtained from

$$\frac{T}{\rho V^2 A_D} = 2\left(\frac{\langle V_d\rangle}{V}\right)\left(\frac{\langle V_d\rangle}{V}-1\right). \tag{5}$$

Given a known $T$, Equations (4) and (5) reveal that a reduction in $A_D$ leads to an increase in $P$, which in turn necessitates a greater battery mass. To avoid installing a heavy battery pack, a smaller $N_{prop}$ is therefore favoured to reduce the required power output, and $N_{prop}$ is observed to be inversely proportional to $EC_{pk}$ at $V = 100$ km/h.

At higher speeds, this design preference is reversed where minimal $EC_{pk}$ is observed at $N_{prop} = 10$. The change in design preference is attributed to the desire to minimize cruise drag, which dominates the energy consumption during cruise and is a significant contributor to the battery weight/MTOM. In the design algorithm, the angle of attack of the wing is adjusted in aim to produce sufficient lift that matches the vehicle's weight and is coupled with the cruise drag. Decreasing the MTOM/lift is found to be an effective strategy for reducing cruise drag. When the reliance on propeller for lift production is reduced with increasing $V$, a smaller MTOM is preferred. Fig. 2 shows that a greater $N_{prop}$ is favoured at $V \geq 150$ km/h since $N_{prop}$ and total propeller weight/disk area are inversely related [24]. An exception is noted at $R = 100$ km and $V = 300$ km/h, where the minimal $EC_{pk}$ is observed at $S = 11$ m$^2$ and $N_{prop} = 8$ rather than $N_{prop} = 10$. A comparison of $EC_{pk}$ between the two configurations reveals that the difference of $EC_{pk}$ is less than $4 \times 10^{-3}$%, indicating the outlier is insignificant to the pattern. In fact, Fig. 2 shows that varying $N_{prop}$ has little influence on $EC_{pk}$ ($< 6$%) at $V \geq 200$ km/h. Significant impact on $EC_{pk}$ from varying $N_{prop}$ is only observed at $V = 100$ km/h, e.g., increasing $N_{prop}$ from 4 to 10 amplifies the level of $EC_{pk}$ by approximately 400% when $R = 250$ km.

The influence of $S$ on $EC_{pk}$ is also revealed in Fig. 2. At low operating speed ($V = 100$ km/h), $EC_{pk}$ is negatively correlated with $S$. The vehicle favours a wing with greater $S$ despite the variation in $R$. As previously discussed, this is attributed to the multicopter characteristic of the vehicle at low operating speeds: the wing is incapable of producing sufficient lift to counter the vehicle's weight. Consequently, The design algorithm aims for a wing with a larger $S$ that can produce more lift. An intuitive interpretation is demonstrated by the contours corresponding to $V = 150$ km/h and $R = 150$, 200, and 250 km. In each of these contours, where $R$ and $V$ are fixed, the level of $EC_{pk}$ is shown to be inversely proportional to $S$.

As $V$ increases to 200 km/h, the design preference on $S$ becomes more complicated. At $R = 150$ km, 200 km, and 250 km, the local minimal $EC_{pk}$ appears at $S = 15$ m$^2$. The design gradually shifts towards favouring smaller $S$ as $R$ reduces to 50 km. This trend indicates that the necessity of wing-based lift is not strong at this speed, and a smaller $S$ is preferred to produce less cruise drag (higher aspect ratio). The local minimal $EC_{pk}$ is consistently observed at $S = 11$ m$^2$ for $V > 200$ km/h. When the minimal $EC_{pk}$ is found at $S = 19$ m$^2$, the vehicle tends to rely on the propeller for lift production. The extent of reliance is proportional to the level of $EC_{pk}$ for vehicles designed with same $R$. It is also worth mentioning that a higher $V$ does not always lead to reducing $EC_{pk}$. Despite the variations in $N_{prop}$ and $S$, the level of contour at $V = 300$ km/h and $R = 50$ km is higher than at $V = 150$ km/h. For $R = 50$ km, it is observed that the level of $EC_{pk}$ rises with increasing $V$, as a greater operating speed requires higher power. It is also of interest to note that a vehicle designed for shorter $R$ (50 km) with a lighter battery pack exhibits a higher level of $EC_{pk}$ compared to those designed for extended $R$, at $V \geq 200$ km/h. This misleading observation can be attributed to the normalization effect relative to $R$. As detailed in Section 2.1, the vehicle is designed to carry additional battery mass to accommodate a 20-min loiter as required by FAA. A smaller $R$ value tends to intensify the adverse effect of this additional weight on $EC_{pk}$.

Given the close association between noise level and community acceptance of UAM [13,14], the impact of $S$ and $N_{prop}$ on the sound power levels of vehicle during takeoff ($PWL_t$) and cruise ($PWL_c$) are evaluated for different $R$ and $V$. The corresponding results are presented in Fig. 3 and 4, respectively. Similar to Fig. 2, Fig. 3 and 4 each consists of 25 contours, corresponding to 25 operating scenarios defined by $R$ and $V$. Each figure presents a total of 500 representative vehicle data. The PWL contours are arranged and annotated following the style of Fig. 2, with the local minimum of each contour being highlighted in red-bordered box. The assessment of $PWL_t$ determines that $PWL_t$ ranges between approximately 75 dBA to 160 dBA, with the level of $PWL_t$ at $V = 100$ km/h typically higher than at other speeds. Similar to Fig. 2, the depicted range of $PWL_t$ in Fig. 3 is capped up to 125 dBA for visualizing the variation of $PWL_t$ at $V > 100$ km/h.

The contours of $PWL_t$ reveal that the values of $PWL_t$ are proportional to $N_{prop}$ throughout all the explored operating scenarios. As previously noted that $A_D$ and $N_{prop}$ are negatively correlated. The observation is therefore attributed to the inverse relation between the rotational speed $\Omega$ of propeller and disk size $A_D$ as detailed in the following equation. Assuming a pitch-controlled propeller blade operating for sustaining maximum total lift coefficient $C_L$ of the sections, $\Omega$ can be determined using $T$ and $A_D$ as [36]:

$$\Omega = 2\sqrt{\frac{6T}{\rho s A_D C_L D^2}}. \tag{6}$$

Note the term $s$ and $D$ from Equation (6) represent the solidity and diameter of the disk, respectively. The equation indicates that a smaller disk results in a higher rotational speed, leading to a larger blade passing frequency (BPF). Here, BPF is defined by $\frac{B\Omega}{2\pi}$ with $B$ representing the number of blades. With increasing BPF, the tonal noise becomes more significant as the A-weighting effect on resulted PWL is attenuated. As a result, the local minimum of $PWL_t$ (red-bordered boxes) is consistently observed at $N_{prop} = 4$ (low RPM) and is independent from $R$ and $V$. Fig. 3 shows that decreasing $N_{prop}$ from 10 to 4 can reduce $PWL_t$ by approximately 20 dBA.

When comparing to the influence of $N_{prop}$, $S$ shows less impact on varying $PWL_t$ in the explored range of this investigation. A weak negative correlation between $S$ and $PWL_t$ is seen in all the contours, where increasing wing area reduces the takeoff noise. Across the operating scenarios demonstrated in Fig. 3, a larger $S$ is consistently favoured with the local minimum of $PWL_t$ always occurs at $S = 19$ m$^2$. This is attributed to the inverse relation between $S$ and wing mass. Since the wing span is fixed in this investigation, a wing with a smaller $S$ (higher AR) tends to be heavier due to the need for increased structural strength. The estimation of wing mass is based on Cessna method [24], which shows that the weight of a cantilevered wing is a function of $S^{0.360}$ and $AR^{1.712}$ (in imperial unit), i.e., AR plays a more important role compared to $S$. Therefore, a larger $S$ leads to a smaller MTOM, which contributes to mitigating takeoff noise.

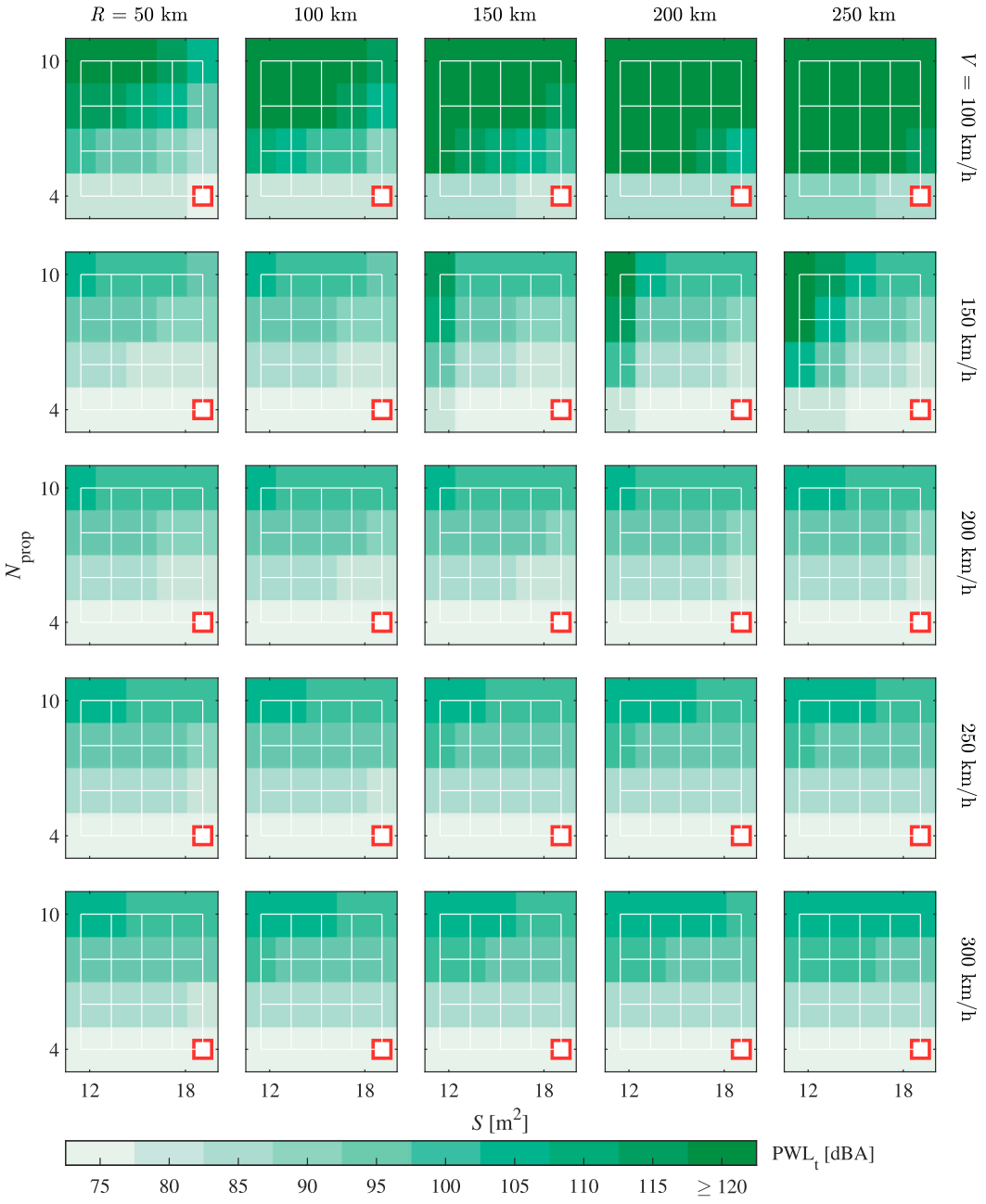


**Fig. 3.** Contours of the sound power level in takeoff ($PWL_t$) with varying $N_{prop}$ and $S$, across different operating scenarios defined by $V$ and $R$. The configuration corresponding to local minimum (within the contour) is highlighted by red-bordered box.

Next, the contours of $PWL_c$ with respect to $N_{prop}$ and $S$ are depicted in Fig. 4 for different operating scenarios. The values of $PWL_c$ range approximately between 40 dBA and 160 dBA, with the displayed range capped at 120 dBA (following the approach in Fig. 3). The influence of $N_{prop}$ on $PWL_c$ is consistent with its influence on $PWL_t$, where a positive correlation is seen between $N_{prop}$ and $PWL_c$. The preferred configuration is found to be $N_{prop} = 4$ across all presented operating conditions. As previously explained, this is attributed to the positive relation between $\Omega$ and $N_{prop}$. A greater $N_{prop}$ leads to a smaller $A_D$, and a higher rotational speed/noise. Decreasing $N_{prop}$ from 10 to 4 can reduce $PWL_c$ by at least 10 dBA.

The relation between $S$ and $PWL_c$ exhibits a similar trend to that observed in Fig. 2 (contours of $EC_{pk}$), where the local minimal $PWL_c$ shifts from $S = 19$ m$^2$ to 11 m$^2$ with increasing $V$. Here, the design preference of $S$ shows two different patterns with respect to $V$. At $V < 200$ km/h, an inverse relation is seen between $S$ and $PWL_c$. As noted earlier, the vehicle at low speeds exhibits characteristics more akin to a multicopter than tilt-rotor aircraft, with its cruise thrust also responsible for lifting the vehicle. Reducing wing weight appears to be effective in mitigating the cruise noise as $T$ is largely affected by MTOM. At $V > 200$ km/h, $PWL_c$ is proportional to $S$. This relation arises because the propeller thrust is solely responsible for overcoming cruise drag, which is reduced with a smaller $S$. At $V = 200$ km/h, some minor fluctuations are detected in the relation between $S$ and $PWL_c$ across $R$. However, the differences in $PWL_c$ due to increasing $S$ from 11 m$^2$ to 19 m$^2$ are on the order of 0.1 dBA, indicating the contribution of $S$ towards $PWL_c$ is negligible. It is also noticed that increasing $V$ beyond 150 km/h elevates the level of $PWL_c$ minima. The local minima of $PWL_c$ at $V = 300$ km/h are approximately 48 dBA. Conversely, at $V = 150$ km/h, the minima of $PWL_c$ range between 38 dBA and 41 dBA with increasing $R$. Nevertheless, the level of $PWL_c$ minima is approximately 30 dB lower than that

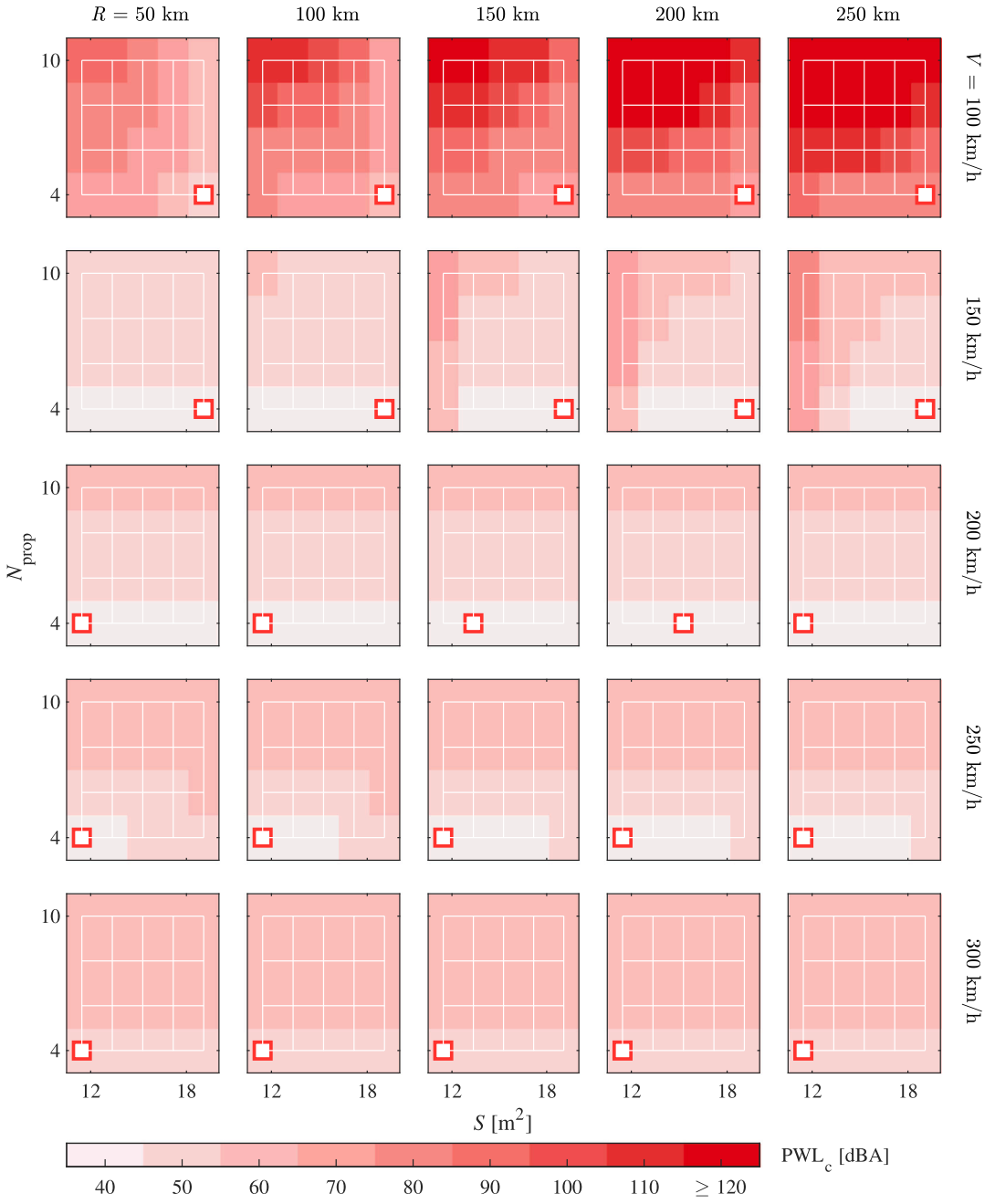


**Fig. 4.** Contours of the sound power level in cruise ($PWL_t$) with varying $N_{prop}$ and $S$, across different operating scenarios defined by $V$ and $R$. The configuration corresponding to local minimum (within the contour) is highlighted by red-bordered box.

of $PWL_t$, highlighting the advantage of tilt-rotor architecture in cruise over multicopter.

Another important aspect of design to investigate is the commercial viability of UAM operation. For such purpose, the impact of adjusting $N_{prop}$ and $S$ on the operating expense per passenger-kilometer ($OE_{pk}$) is evaluated. The results corresponding to various operation conditions are presented in the contours from Fig. 5. The local minimum of each contour is marked by red-bordered box, and the figure is annotated similarly to Fig. 2, 3, and 4. It is determined that $OE_{pk}$ ranges over approximately 0.4 €/pax/km to 17 €/pax/km. Mirroring the approach in Fig. 2, the illustrated range of $OE_{pk}$ in Fig. 5 is limited up to 2.2 €/pax/km to help visualize the variation of $OE_{pk}$ at $V > 100$ km/h.

Fig. 5 suggests that the influence of adjusting $N_{prop}$ on $OE_{pk}$ is mostly observed at $V \leq 150$ km/h, while no clear dependency is found between the two values at higher speeds. Although the displayed range is capped at 2 €/pax/km, the result reveals a strong positive correlation between $N_{prop}$ and $OE_{pk}$ at $V = 100$ km/h, especially when $S$ is small. As a result, $N_{prop} = 4$ appears to be the preferred design choice. This is associated with the high energy consumption during cruise, as the vehicle acts like a multicopter at low speed. At $V > 100$ km/h, Fig. 5 shows that a large $N_{prop}$ is favoured. The flip in design preference is due to the overall weight and installed power reduction by increasing $N_{prop}$, which leads to lower total mass and power consumption.

Similar to the results with $N_{prop}$, Fig. 5 reveals that the influence of $S$ on $OE_{pk}$ is mainly detected at $V \leq 150$ km/h. It is found that $S$ and $OE_{pk}$ are inversely related at low speeds, and $S = 19$ m$^2$ is always favoured. As previously explained, this is attributed to the fact that at low-speed cruising, propellers are responsible for lifting the vehicle, which consumes a notable amount of energy and leads to higher energy costs. A larger $S$ is therefore desired to minimize $OE_{pk}$. The extent of dependence

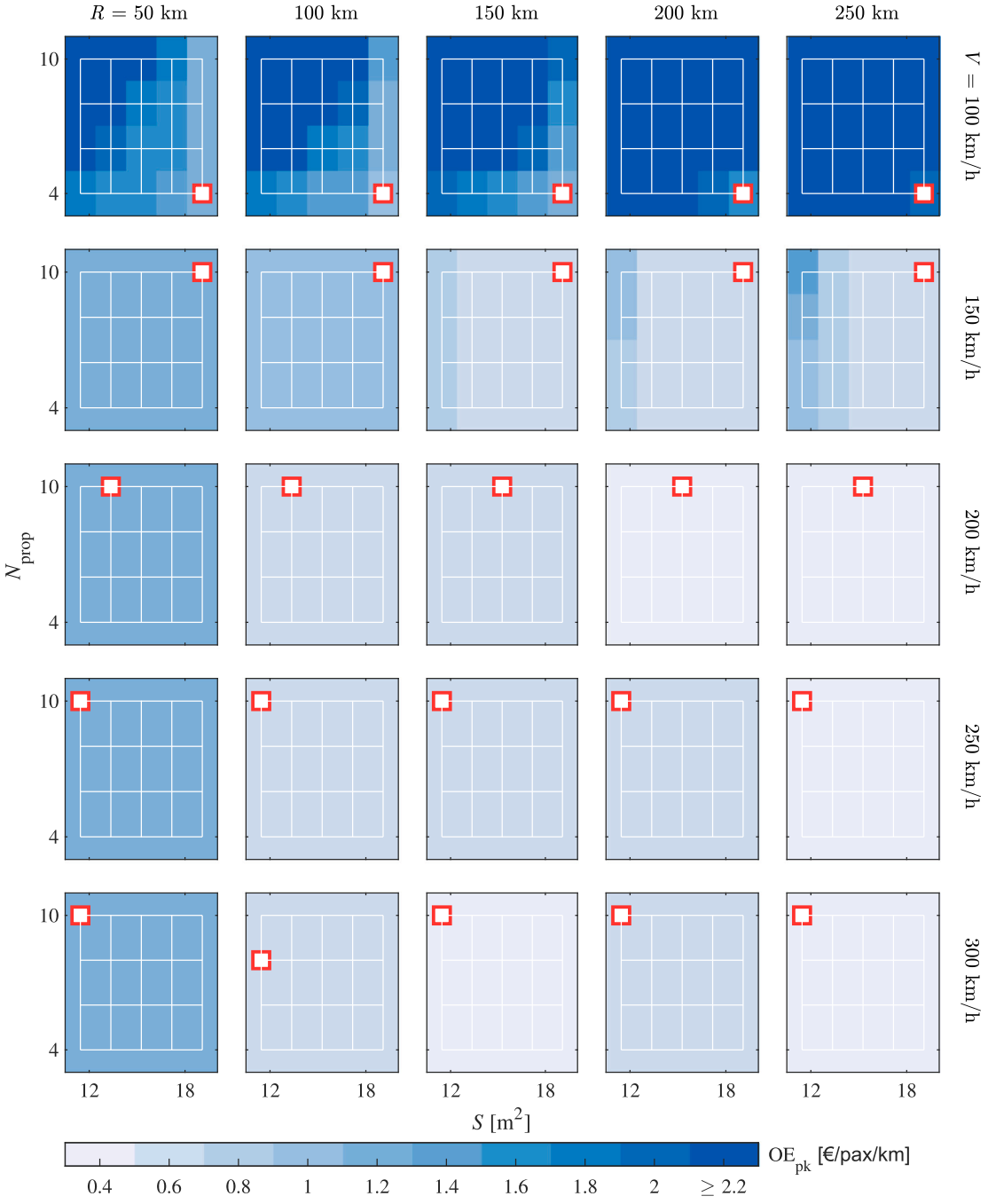


**Fig. 5.** Contours of the operating expense per pax-km ($OE_{pk}$) with varying $N_{prop}$ and $S$, across different operating scenarios defined by $V$ and $R$. The configuration corresponding to local minimum (within the contour) is highlighted by red-bordered box.

between $S$ and $OE_{pk}$ appears to grow with increasing $R$, highlighting the importance of wing-generated lift in long-range operations. The preference on $S$ gradually shifts towards favouring a smaller $S$ with increasing $V$. This is associated with the coupling between wing weight and cruise drag, whereas a smaller $S$ tends to produce less drag.

At $R = 50$ km, the overall level of $OE_{pk}$ in each contour is seen to be higher than the rest of the contours at $V > 150$ km/h. However, $OE_{pk}$ of each contour does not exhibit an obvious increase with rising $V$, which is different from the observation regarding $EC_{pk}$ (Fig. 2). Notable variations in the overall level of $OE_{pk}$ are observed with increasing $R$ for $V > 150$ km/h, which also differs from the results derived from Fig. 2. These discrepancies suggest that the main contributor to the overall $OE_{pk}$ is not the energy cost, but rather the personnel cost that is proportional to the flight hours. Further discussion regarding the composition of OE is provided in the subsequent section.

### 3.2. Performance variables

This section builds upon the results shown in Section 3.1, and further explores the relation between performance variables and energy consumption, noise emission, and commercial viability. The performance variables are defined by $V$ and $R$ with optimal cases identified using design filters. The analysis is compared against several vectored-thrust vehicles: Joby S4 (pre-production prototype, Joby Aviation), VA-X4 (Vertical Aerospace), and Lilium 5-seater (Lilium GmbH) by plotting their performance parameters in the same contour. Additionally, the VoloCity (Volocopter GmbH), which utilizes multicopter architecture,

is also considered for the purpose of comparison. Note the performance data of these vehicles are sourced from publicly available information, and should only be used to guide the discussions rather than for direct comparisons.

In terms of environmental impact due to energy consumption, EC is employed as a design filter. Specifically, for each $R$ and $V$, the vehicle with the minimum value of EC is considered as the optimal design when varying $S$ and $N_{prop}$. The contours of the minimal energy consumption are presented in Fig. 6, on a grid defined by $V$ and $R$. The trend of total energy consumption per flight is illustrated in Fig. 6 (a) in the contour of minimal $EC_p$. The result reveals that the majority of operating conditions yield an $EC_p$ within the range between 10 kWh/pax and 90 kWh/pax, with the minimum $EC_p$ is observed at $R = 25$ km and $V = 125$ km/h. The overall pattern suggests that the level of $EC_p$ rises progressively as $V$ and $R$ increase, with an exception noted at low operating speed. At $V < 125$ km/h, notable increase in $EC_p$ is observed as $R$ extends, in particularly at $R > 100$ km. As previously discussed, the observed phenomenon is attributed to a shift in the vehicle's lifting characteristics when $V$ surpasses a speed threshold, which is found to be between 125 km/h and 175 km/h, depending on the operating range. The observation matches the performance parameters of the referenced vehicles, which are shown in the same grid using black dots. To facilitate the comparison of EC across various $R$, the contour of minimal energy consumption per passenger-km ($EC_{pk}$) is demonstrated in Fig. 6 (b), which is assembled from the local minima of $EC_{pk}$ from Fig. 2. It serves the purpose of identifying the optimal operating parameters in terms of $EC_{pk}$. The contour exhibits a different pattern than the one observed in Fig. 6 (a). Fig. 6 (b) reveals that a tipping point exists with increasing $R$, and the minimal $EC_{pk}$ of 0.12 kWh/pax/km is detected at $R = 200$ km and $V = 125$ km/h. For short-range operations, the dependency between $V$ and $EC_{pk}$ appears to be stronger when comparing to the contour of $EC_p$ from Fig. 6 (a), indicating the short-range operations are more energy demanding per km.

Overall, low operating speeds are preferred from the perspectives of both $EC_p$ and $EC_{pk}$, although a minimum speed of 125 km/h is necessary to effectively reduce the reliance on propellers for sustaining level flight. The total energy consumed per flight exhibits moderate elevation with extending $R$ for tilt-rotor vehicles. Without taking flight frequency into account, short-range operations are preferred in terms of $EC_p$. Conversely, energy consumption per km tends to be lower at extended ranges since the impact of mission stages other than cruise is minimized. It is important to note that the performance variables of the reference vehicles do not fall within the low-emission ($EC_{pk}$) zone. This discrepancy can be attributed to the differences between the assumed battery energy density (585 Wh/kg) [8,9] and the current one (approximately 200 Wh/kg) [40].

The PWLs of vehicle during takeoff and cruise are evaluated across the grid defined by $R$ and $V$. Similar to the results presented in Fig. 6, the minimal PWLs at each grid point are identified by exploring $S$ and $N_{prop}$, and the results of minimal $PWL_t$ and $PWL_c$ are shown in Fig. 7 (a) and (b), respectively. Fig. 7 (a) demonstrates that $PWL_t$ is proportional to $R$ and $V$, aligning with the observation of Fig. 6 (a). For extended $R$ and higher $V$, a heavier battery pack is necessitated due to the increase in energy consumption. Consequently, the propellers tend to operate at higher rotational speed to compensate for the increased lift demand, leading to elevated noise. Similar to Fig. 6 (a), the level of $PWL_t$ rises dramatically with increasing $R$ at $V = 100$ km/h. At $V > 100$ km/h, most operating scenarios have a takeoff PWL less than 76 dBA, while $PWL_t$ reaches approximately 89 dBA at $V = 100$ km/h and $R = 300$ km. The minimal $PWL_t$ values are observed in the light-green contour region, approximately 75 dBA, with differences on the order of 0.1 dBA across the grid.

In contrast to Fig. 7 (a), Fig. 7 (b) indicates that the level of $PWL_c$ exhibits little dependency on $R$ at $V > 100$ km/h. This discrepancy, with respect to Fig. 7 (a), is due to the fact that propellers mainly need to produce sufficient thrust to overcome the cruise drag, which does not vary significantly despite the increase in battery weight from extending $R$. Similar to Fig. 7 (a), the cruise noise is also observed to be proportional to $V$, as greater thrust and higher RPM are expected at higher $V$. For operations at $V > 100$ km/h, the level of $PWL_c$ is generally seen below 50 dBA, which is significantly lower than the level of $PWL_t$ at the same speeds. The variation in $PWL_c$ within the light-red contour region is insignificant. The minimal $PWL_c$ is mainly observed between $V = 125$ km/h and 200 km/h, with value around 40 dBA. For operations at $V = 100$ km/h, $PWL_c$ is seen to elevate with increasing $R$ and reaches 84 dBA at $R = 300$ km. At this low speed, the cruise PWL gradually converges to the value of takeoff PWL with extending $R$. The trend is attributed to the increasing reliance on propellers for lift production, with the propellers eventually operating at similar rotational speeds during both takeoff and cruise. It is found that the rotational speeds during cruise increase from 87 RPM to 249 RPM as $R$ extends from 25 km to 300 km. The latter RPM value is comparable to the takeoff RPM (281 RPM) found at the same $R$ of 300 km. Here, it is worth reminding that the reported ideal PWLs in Fig. 7 correspond to configurations with $N_{prop} = 4$ operating at low RPMs. When more smaller propellers are employed, the takeoff RPMs exceed 1000 RPM.

In addition to the elevation in overall cruise PWL, it is worth mentioning that the balance between the tonal and broadband components shifts with increasing $R$ at $V = 100$ km/h. This is associated with the wide range of rotational speeds observed across explored $R$. Previous work by the authors [19] demonstrated that both tonal and broadband noises (A-weighted) of tilt-rotor vehicle are significant when the propellers operate at high RPM. In contrast, only broadband noise is significant when propellers operate at low RPM. The prominence of tonal noise appears to be proportional to the rotational speed, as the A-weighting benifit diminishes with increasing BPF. Note that the perception and level of annoyance differ between tonal and broadband noises, with the tonal component of transportation noise generally considered more annoying [41]. Due to the absence of major tonal components, the investigated vehicles in cruise are more ideal than conventional aircraft and helicopters.

Overall, reducing the rotational speed of propellers can decrease noise during both takeoff and cruise. A short operating range with a light battery is preferred for mitigating takeoff noise, while operating at low speeds is favoured for reducing cruise noise. The lowest level of $PWL_c$ is at least 30 dBA lower than the minimum $PWL_t$ across $R$. This difference illustrates one important advantage of tiltrotors against multicopter architectures. By relying on the wing for lift during cruise, noise emissions are significantly reduced, offering a competitive advantage for operations over cities and densely populated areas.

The influence of performance variables on the commercial viability of the vehicle is assessed using the design filter operating expense (OE). For each operating condition, minimal $OE_p$ and $OE_{pk}$ are determined from exploring $S$ and $N_{prop}$. The resulted contours are illustrated in Fig. 8 (a) and (b), respectively. Note the former contour indicates the operating expense per passenger for a full-range flight, while the latter contour enables a fair comparison of the operating cost across $R$. The contour of $OE_p$ demonstrates a pattern that is different from the contour of $EC_p$ shown in Fig. 6 (a). A positive correlation between $OE_p$ and $R$ is seen across all explored $V$, while this correlation weakens as $V$ increases. Minor fluctuations are detected at $R = 150$ km, 175 km, and 300 km and are attributed to the effect of superimposing energy cost and personnel cost, which is further discussed in the subsequent text associated with Fig. 9.

Fig. 8 (b) presents the contour of ideal $OE_{pk}$, with the local minimum value highlighted using red dots for the respective $R$. The observed relations between $OE_{pk}$ and performance variables differ significantly from those between $EC_{pk}$ and parameters $R$ and $V$. High $OE_{pk}$ values ($\geq 1$ €/pax/km) are primarily observed along the grid lines where $V = 100$ km/h and $R \leq 50$ km. With increasing $R$ and $V$, the level of $OE_{pk}$ exhibits a declining trend. Local minima at each $R$, marked by red dots, are observed in a diagonal direction across the grid of $R$ and $V$, form-

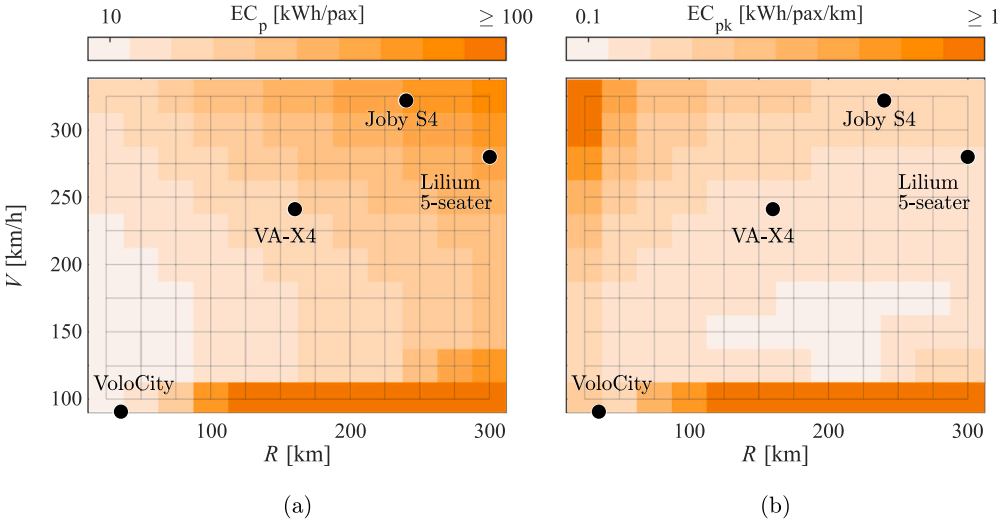


**Fig. 6.** Contours of the optimal energy consumption (a) per pax ($EC_p$) and (b) per pax-km ($EC_{pk}$) across different operating scenarios defined by $V$ and $R$.

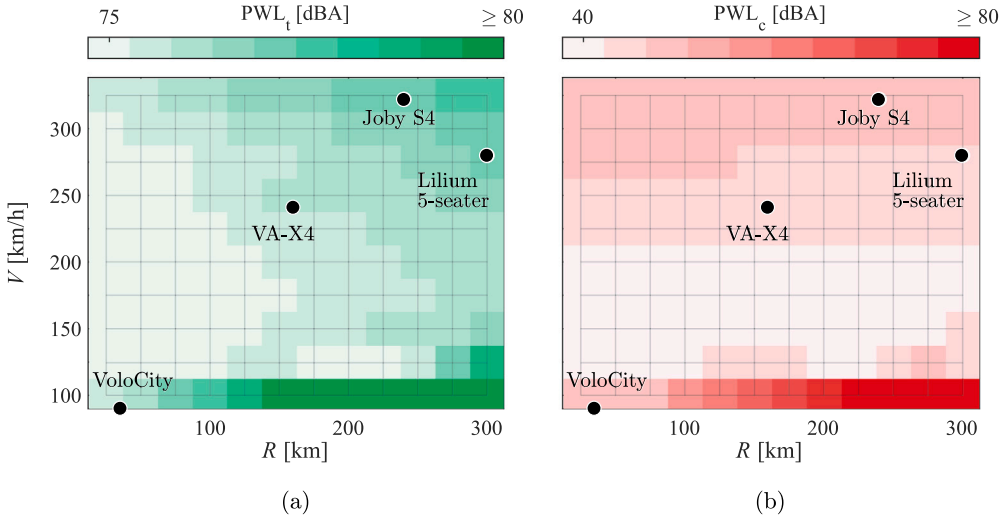


**Fig. 7.** Contours of the optimal sound power level during (a) takeoff ($PWL_t$) and (b) cruise ($PWL_c$) across different operating scenarios defined by $V$ and $R$.

ing two "ladders" at $R \leq 175$ km and $R > 175$ km. Each ladder depicts a relation between $R$ and the corresponding ideal $V$, in terms of optimal $OE_{pk}$. The result shows that the ideal operating speed does not consistently increase with extending $R$, and is likely due to the limitations on explored $V$ and increasing impact of energy consumption.

It is of interest to note that the presented existing tilt-rotor vehicles all fall in a low $OE_{pk}$ zone, between the two ladders. This observation holds true despite the large difference in pack-level energy density between current (≈ 200 Wh/kg) [40] and future projections (585 Wh/kg) [8,9], and further highlights the importance of mission time, as the existing vehicles tend to favour a high operating speed for low flight time and personnel cost. In addition, a high operating speed can render the operation more commercially competitive when comparing to other means of transportation. A vehicle designed to cruise at high speed can also operate at lower speeds for more flexible business models.

To further analyze the patterns observed in Fig. 8, the direct operating costs (DOC) are decomposed into two components: operating expense that are related to personnel cost ($OE_t$), and energy ($OE_{EC}$), with the corresponding contours illustrated in Fig. 9 (a) and (b), respectively. As detailed in Section 2.3, $OE_t$ consists of pilot and maintenance costs, and is determined by the wrap rates and mission time $t$. The wrap rates are considered as fixed constants in this study to simplify the analysis. Hence, $OE_t$ exclusively depends on $t$, which varies with changes in performance variables. Conversely, the energy cost $OE_{EC}$ is a function of both $t$ and the power output of the propulsion system, with the latter also varying according to aircraft design considerations. Fig. 9 (a) depicts a pattern that is near identical to Fig. 8 (b) for the operations with $V > 100$ km/h. Note a shorter mission time typically corresponds to a high cruising speed, implying that the $V$ of optimal $OE_t$ should rise with increasing $R$. The pattern shown in Fig. 9 (a) deviates from this trend, attributing to the limits on the range of explored $V$ and the conservative estimation for personnel cost, where the flight hours are rounded up to the nearest integer. As shown in Fig. 9 (b), the level of $OE_{EC}$ is much lower than $OE_t$ in general, with the maximum contribution of $OE_{EC}$ to $OE_{pk}$ found to be 14% at $R = 300$ km and $V = 325$ km/h. To optimize operating costs, designs for UAM vehicles with tilt-rotor architecture should prioritize on reducing mission time.

In summary, at $V > 100$ km/h, the energy cost is not the major contributor to the overall operating expense per pax-km, regardless of $R$. However, its role is still pivotal in preventing the vehicle from operating at high speeds over extended ranges, as its weight in $OE_{pk}$ increases with both $R$ and $V$. Furthermore, it should be noted that the aforementioned results may vary depending on the level of automation and advanced traffic control, as the personnel cost and mission time are subject to change. For instance, a fully automated operation can reduce $OE_t$ by over 50%, making $OE_{EC}$ more significant. With these changes, the opti-

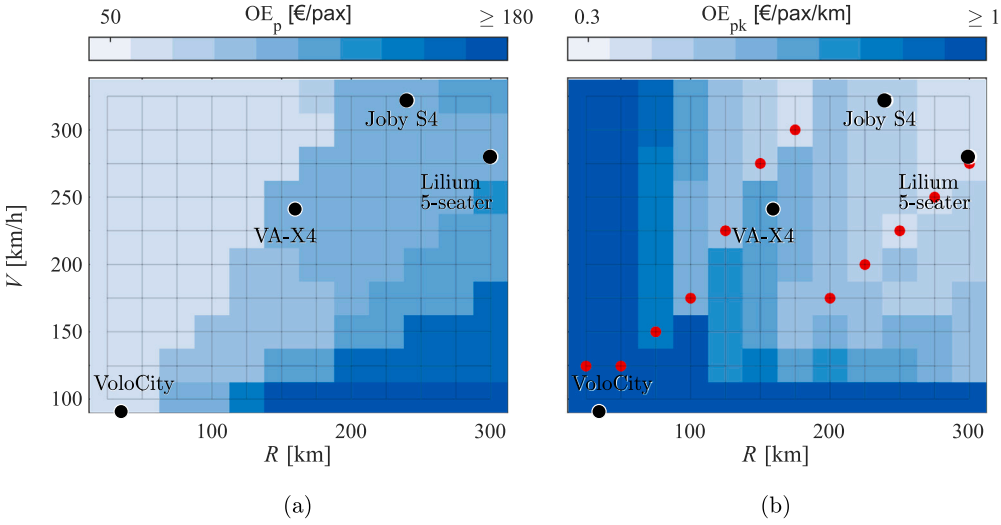


**Fig. 8.** Contours of minimum (a) $OE_{pk}$ and (b) $OE_p$ across different operating scenarios defined by $V$ and $R$.

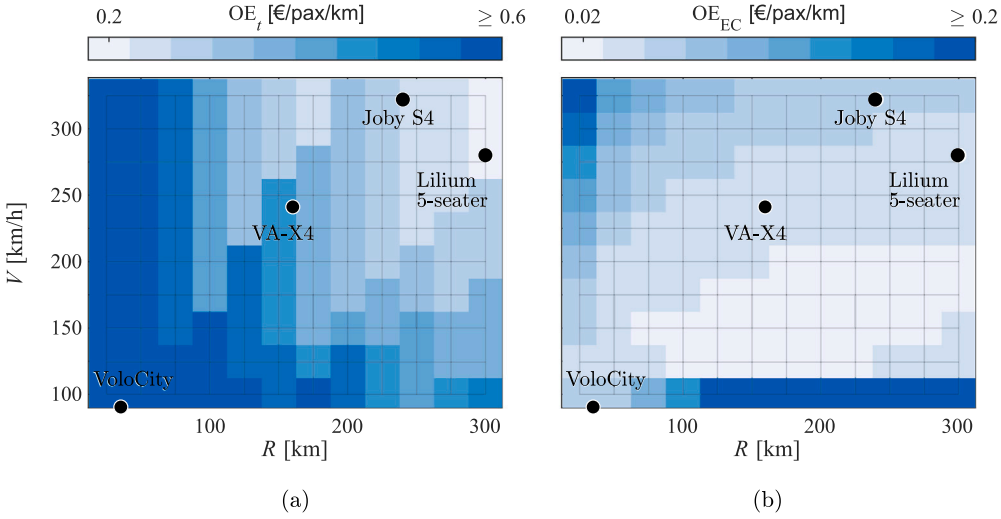


**Fig. 9.** Contours of optimal operating expense due to (a) flight time ($OE_t$) and (b) energy consumption ($OE_{EC}$) across different operating scenarios defined by $V$ and $R$.

mal operating conditions from an economic perspective may align with those from an environmental one. However, it should be noted that the optimal vehicle design relies on combined metrics, with the weighting of metrics such as energy consumption, noise considerations, and commercial viability varying across different objective functions. Accordingly, the definition of the ideal configuration is contingent upon the interests and priorities of the stakeholders.

In addition to the analysis of OE, a preliminary assessment of the development cost ($C_{Dev}$) is carried out. The assessment is performed for the vehicle configurations corresponding to those in Fig. 8, providing more insights into their commercial viability. The model of $C_{Dev}$ is developed within the framework of COLOSSUS project, arising from exploring the Life Cycle Analyzer tool [42–44] developed at Department of Mechanical and Aerospace Engineering, Politecnico di Torino. The model encompasses costs related to research, design, prototyping and flight test. To utilize the cost estimation tool, the systems of the vehicle are categorized into four groups, namely airframe, propulsion, subsystems, and batteries. Here, airframe consists of wing, fuselage, tails, nacelles, and landing gear. The propulsion system encompasses power cables, motors, inverters, and propellers. The subsystems include flight control, avionics, environmental control and electric systems. The derived model of $C_{Dev}$ is driven by the mass of components, which allows to capture the cost variations due to configuration differences while using the same technology. The development costs for the systems of airframe, propulsion, and subsystems are described in euros using the following equations,

$$C_{\text{Airframe}} = 138,242 m_{\text{Airframe}} + 40,497,006, \tag{7}$$

$$C_{\text{Propulsion}} = 188,712 m_{\text{Propulsion}} + 35,368,406, \tag{8}$$

$$C_{\text{Subsystems}} = 758,893 m_{\text{Subsystems}} + 110,390,174, \tag{9}$$

with the component masses denoted by $m_{\text{Airframe}}$, $m_{\text{Propulsion}}$, and $m_{\text{Subsystems}}$. The mass information is obtained through the second-order mass estimation using the design tool [19]. Due to the preliminary nature of the tool, detailed information on the masses of subsystems is not available. The overall $C_{Dev}$ is then estimated using

$$C_{\text{Dev}} = C_{\text{Airframe}} + C_{\text{Propulsion}} + C_{\text{Subsystems}}. \tag{10}$$

Note the development cost for batteries is neglected here as they are treated as off-the-shelf products within the COLOSSUS project.

The contour of $MTOM_{OE}$ corresponding to the configurations shown in Fig. 8 (b) are first presented in Fig. 10 (a) as the weight of the vehicle is the main driver for carrying out a development cost analysis. Fig. 10 (a) shows that the MTOM of the configurations with ideal $OE_{pk}$ gener-

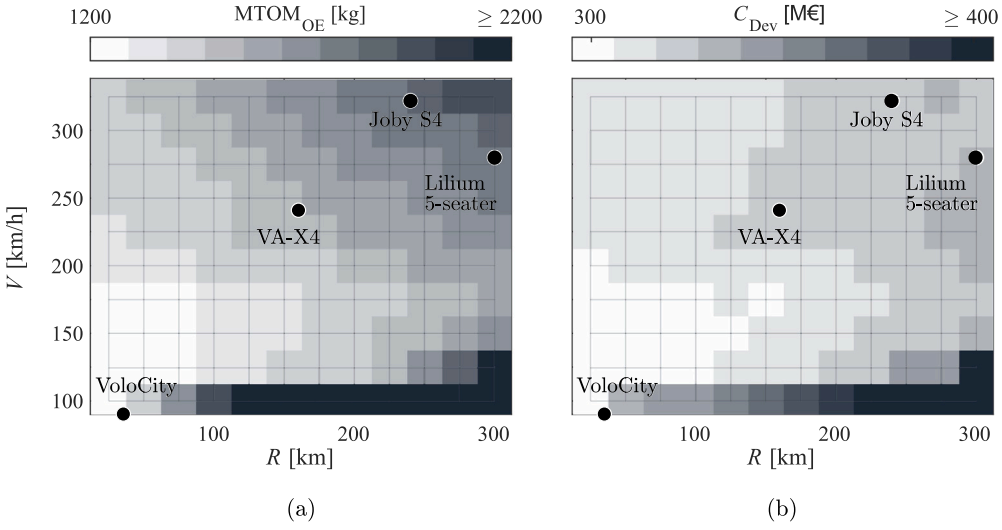


**Fig. 10.** Contours of (a) maximum takeoff mass of vehicles with ideal $OE_{pk}$ ($MTOM_{OE}$), and (b) the development cost in million euros ($C_{Dev}$) across different operating scenarios defined by $V$ and $R$.

**Table 6**
Brief summary of vehicle configurations with ideal $OE_{pl}$ at different operating conditions, defined by $V$ and $R$.

| $R$ | $V$ | $S$ | $N_{prop}$ | PL | DL | MTOM | $OE_{pk}$ | $PWL_t$ | $PWL_c$ |
|---|---|---|---|---|---|---|---|---|---|
| [km] | [km/h] | [m$^2$] | - | [kg/kW] | [kg/m$^2$] | [kg] | [€/pax/km] | [dBA] | [dBA] |
| 25 | 125 | 19 | 10 | 1.46 | 82.6 | 1,203 | 2.31 | 97 | 54 |
| 50 | 125 | 19 | 10 | 1.44 | 81.8 | 1,231 | 1.17 | 97 | 54 |
| 75 | 150 | 19 | 10 | 1.44 | 82.0 | 1,255 | 0.79 | 97 | 54 |
| 100 | 175 | 16 | 10 | 1.50 | 84.6 | 1,326 | 0.60 | 98 | 54 |
| 125 | 225 | 11 | 10 | 1.68 | 94.9 | 1,482 | 0.50 | 104 | 56 |
| 150 | 275 | 11 | 10 | 1.81 | 101.7 | 1,586 | 0.44 | 105 | 60 |
| 175 | 300 | 11 | 10 | 1.88 | 106.1 | 1,666 | 0.39 | 106 | 61 |
| 200 | 175 | 19 | 10 | 1.44 | 81.4 | 1,426 | 0.49 | 98 | 54 |
| 225 | 200 | 14 | 10 | 1.55 | 87.5 | 1,528 | 0.44 | 101 | 56 |
| 250 | 225 | 11 | 10 | 1.68 | 94.9 | 1,658 | 0.41 | 105 | 57 |
| 275 | 250 | 11 | 10 | 1.76 | 99.3 | 1,726 | 0.38 | 106 | 58 |
| 300 | 275 | 11 | 10 | 1.85 | 104.9 | 1,820 | 0.36 | 107 | 60 |

ally falls in between 1,200 kg and 2,200 kg, when $V$ is greater than or equal to 125 km/h. The results corresponding to $V = 100$ km/h further prove that the tilt-rotor architecture is inadequate for extended-range operation at such low speed. The values of $MTOM_{OE}$ at $R > 150$ km are significantly higher than the rest of the cases and are an order of magnitude higher than 2,200 kg at $R = 300$ km. In general, the values of $MTOM_{OE}$ increase with both increasing $V$ and extending $R$. Some exceptions are noted at $R > 200$ km, where the trend of $MTOM_{OE}$ exhibits fluctuations, with values falling and rising with increasing $V$. The pattern largely resembles that of Fig. 6 (a) (total EC per flight), indicating the weight of battery plays an important role in the variations of MTOM.

Next, the results of $C_{Dev}$ corresponding to the configurations presented in Fig. 8 (b) is illustrated in Fig. 10 (b), where the contour levels are expressed in units of million euros (M€). The level of $C_{Dev}$ for $V >$ 125 km/h is observed to be approximately between 300 M€ to 330 M€ at $V > 100$ km/h. The pattern does not fully align with that observed in Fig. 10 (a) as the battery is neglected when estimating $C_{Dev}$. The contour shows that increasing $R$ generally elevates $C_{Dev}$ at $V > 100$ km/h. The response of $C_{Dev}$ due to increasing $V$ is more complicated and is attributed to the modulations in component weight, driven by the design preference presented in Fig. 5. Upon examining the estimated weight of each component, it is observed that the propulsion systems are heavier at low operating speeds and long operating ranges, as those designs feature a few large propellers to reduce energy consumption. In contrast, the wing component is heavier when the vehicle is utilized for high-speed cruising, where a smaller aspect ratio (AR) wing is employed. As previously discussed, opt for a thinner wing with smaller wing area helps reduce cruise drag; however, this will result in a heavier wing to maintain structural strength. Nevertheless, at $V > 100$ km/h, increasing $R$ and $V$ leads to minor variations (30 M€) in $C_{Dev}$, despite the $MTOM_{OE}$ increasing from 1,200 kg to 2,200 kg. The influence of $MTOM_{OE}$ on $C_{Dev}$ is deemed insignificant for the range of weights explored.

### 3.3. Discussion on design preference

A brief summary of the performance specifications for the vehicles with minimal $OE_{pk}$ at different $R$ is presented in Table 6. Note that these design configurations correspond to the red dots shown in Fig. 8 (b), which are deemed as the most commercially viable vehicle for the respective $R$. The summary includes their attributes such as the ideal $V$, $S$, $N_{prop}$, $PWL_t$, $PWL_c$, power loading (PL), disk loading (DL), MTOM, and $OE_{pk}$. Here, the PL and DL are defined by the ratio between MTOM and total installed power and total rotor disk area, respectively. Table 6 offers a comprehensive overview of the specifications for eVTOL vehicles with tilt-rotor architecture, designed for UAM and RAM operations.

As seen in Table 6, the ideal $V$ does not increase continuously with extending $R$ across the explored operating ranges. This is attributed to the balance of energy cost and mission time-related cost, as previously discussed (Fig. 9). A higher $V$ can effectively reduce mission time and personnel cost, but it also requires increased energy input. In addition, the conservative estimation on mission hours diminishes some of the minor advantages in reducing personnel cost due to increasing speed. Next,

the trend in $V$ with increasing $R$ is negatively correlated with the trend of $S$. As explained in Section 3.1, this relation arises from the balance between lift contribution due to $V$ and $S$. The design preference on $N_{prop}$ indicates that installing more propellers is more favourable irrespective of $R$. This is attributed to the fact that the reliance on lift support from propellers is minimized when the vehicles operate at the ideal $V$. Having more propellers can reduce the energy consumption during cruise while maintaining fail-safe considerations for motor malfunction.

The values of PL and DL are presented in Table 6 to illustrate the efficiency in utilizing power and rotor disk. Note that the propulsion system was sized based on MTOM and total installed power, and is tailored for the takeoff stage [19]. These values are thus key indicators reflecting the vertical flight capability. In general, the PL and DL of a rotorcraft are inversely related for a given MTOM due to the relation of $P/T \propto \sqrt{T/A_d}$ [39,45,46]. A high PL results in a small DL, corresponding to efficient vertical flight. Conversely, the cruise stage favours a high DL to reduce cruising power since the required thrust is a fraction of MTOM and the axial velocity is much higher than that of hovering [46]. However, this inverse relation between PL and DL is not seen in Table 6 as the vehicles exhibit notable variations in the MTOM with increasing $R$. It is verified that both PL and DL are positively correlated with the MTOM, indicating that the hovering and aerodynamic efficiencies of tilt-rotor vehicles are linked to their lifting capability. Hence, a direct comparison of PL and DL across a wide range of MTOM does not offer much insight into the hovering and aerodynamic efficiencies. For the explored $R$, the MTOM of vehicles approximately ranges from 1,200 kg to 2,200 kg as $R$ increases, with minor fluctuations observed at $R$ = 200 km due to variations in $V$. The phenomenon is associated with changes in battery mass, as operations over longer ranges typically consume more energy, whereas lower cruise speeds generally require less energy. It's worth mentioning that the inverse relation between PL and DL is observed when vehicles with similar MTOMs are compared, such as when varying the $N_{prop}$ of vehicles designed for the same $R$ and $V$.

The $OE_{pk}$ of shorter-range operations are found to be on the higher side. For the operations at $R$ = 25 km and 50 km, the minimal $OE_{pk}$ are determined to be 2.31 €/pax/km and 1.17 €/pax/km, respectively. Using $OE_{pk}$ = 0.4 €/pax/km as a threshold (approximately 17% of the minimal $OE_{pk}$ for $R$ = 25 km), Table 6 suggests that mid-range operation ($R$ = 175 km) at high operating speed ($V$ = 300 km/h) and long-range operation ($R$ = 275 km to 300 km) at slightly reduced speed ($V$ = 250 km/h to 275 km/h) are the most commercially competitive options. Concerning the noise level, decreasing $N_{prop}$ can effectively reduce the PWL of vehicle during both takeoff and cruise as shown in Fig. 3 and 4. The corresponding change in $OE_{pk}$ at $V > 150$ km/h, however, is insignificant as the energy cost is not the dominant contributor to operating expense. When $N_{prop}$ is reduced from 10 to 4, it is found that a reduction of up to 25 dBA for $PWL_c$ and up to 14 dBA for $PWL_c$ can be achieved. In summary, the takeoff PWL is observed to be between 97 dBA and 107 dBA across the explored $R$. The variation in $PWL_t$ with increasing $R$ appears to correlate with the changes in $V$ and MTOM, since $V$ influences the battery mass and, consequently, MTOM. The same pattern is also observed for $PWL_c$, while the values of $PWL_c$ are found to be significantly smaller than $PWL_t$.

### 3.4. Noise regression and sensitivity studies

A regression model is derived using the A-weighted PWL results obtained in this exploration. To establish the model, it is essential to first identify the configuration parameters that are critical to the propeller noise. According to Ruijgrok [47], these parameters include shaft power $P_s$, propeller diameter $D$, tip Mach number $M_t$, and number of blades $B$. These parameters were related to the maximum sound pressure level ($SPL_{max}$) of conventional propeller-driven aircraft at far field in the form of [47]

$$\begin{aligned} SPL_{max}(r) = {} & 83.4 + 15.3\log_{10}P_s - 20\log_{10}D + 38.5M_t - 3(B-2) \\ & + 10\log_{10}N_{prop} - 20\log_{10}r, \end{aligned} \tag{11}$$

where the SPLs of propellers are graphically determined [48,49]. Here, $r$ represents the distance from propeller. The value of $P_s$ can be obtained from $\frac{P}{FM}$, where FM is the figure of merit. The blade tip Mach number is defined as $\frac{\pi D \Omega_{RPM}}{60c}$ with $\Omega_{RPM}$ representing the propeller rotational speed and $c$ is the speed of sound in air. Inspired by that, the following equation is proposed to estimate the A-weighted PWL of eVTOL vehicles:

$$PWL = K_P\log_{10}P_s + K_D\log_{10}D + K_M\log_{10}M_t + K_B B + 10\log_{10}N_{prop} + C, \tag{12}$$

with $K_P$, $K_D$, $K_M$, and $K_B$ denote the fitting coefficients that need to be determined and C is a constant. In this context, Equation (12) is no longer dependent on $r$ as the equation computes PWL instead of SPL. A second consideration sets $K_M$ to 60, reflecting the expected velocity dependency of dipolar sources of aeroacoustic noise [50]. Additionally, by directly fitting the A-weighted levels, the effects of decreasing the blade rotational speed and, consequently, modifying human-ear response to the tonal noise are also taken into account. As previously noted, the aforementioned results only consider propellers with $B$ = 5 (following VA-X4 and Joby S4). Thus, extra PWL results are required to help identify the role of $B$ in Equation (12). By including the same parameter sweep realised with $B$ = 3 (matching Airbus Vahana Alpha 2) and 4, $K_P$, $K_D$, $K_B$, and C can be obtained by solving the following system, using a least-squares approximation:

$$\begin{bmatrix} PWL_1 - 10\log_{10}N_1 - 60\log_{10}M_1 \\ \vdots \\ PWL_m - 10\log_{10}N_m - 60\log_{10}M_m \end{bmatrix} = \begin{bmatrix} \log_{10}P_1 & \log_{10}D_1 & B_1 & 1 \\ \vdots & \vdots & \vdots & \vdots \\ \log_{10}P_m & \log_{10}D_m & B_m & 1 \end{bmatrix} \begin{bmatrix} K_P \\ K_D \\ K_B \\ C \end{bmatrix}.$$

In this system, $m$ corresponds to the number of equations/vehicles considered to compute the fitting coefficients. The computation does not include cases with $V \leq 150$ km/h, as many of them exhibit notable reliance on propellers for lift generation, leading to unrealistic MTOM. As a result, a total number of $m$ = 5,040 configurations are considered to determine the fitting coefficients. The inputs $P_s$ and $D$ have unit of watt and meter, respectively. The solidity of propellers is held constant for all the configurations. Upon examining the results of preliminary fitting, it is noted that the coefficients vary with respect to mission stages. This is potentially due to the large difference in disk loading and $\Omega_{RPM}$ between takeoff and cruise. The required thrust and $\Omega_{RPM}$ during cruise are only a fraction of that during takeoff. The computed fitting coefficients corresponding to takeoff and cruise are presented in the following equations

$$\begin{aligned} PWL_{t,re} = {} & 3.2\log_{10}P_s - 20.3\log_{10}D + 60\log_{10}M_t - 2.9B \\ & + 10\log_{10}N_{prop} + 124.1, \text{ and} \end{aligned} \tag{13}$$

$$PWL_{c,re} = 14.1\log_{10}D + 60\log_{10}M_t + 0.5B + 10\log_{10}N_{prop} + 102.2, \tag{14}$$

respectively. The subscript 're' denotes the PWLs are recovered using Equations (13) and (14). Although more precise models [28,51–53] have been previously established, they typically require detailed propeller information and considerable effort to implement [47], which may not be ideal for a preliminary design stage and do not provide direct interpretation on the effects of basic design parameters. In contrast, the proposed regression model offers reliable trends with only basic powertrain information as input, making it ideal for the preliminary design stage and facilitating discussion regarding the design choices.

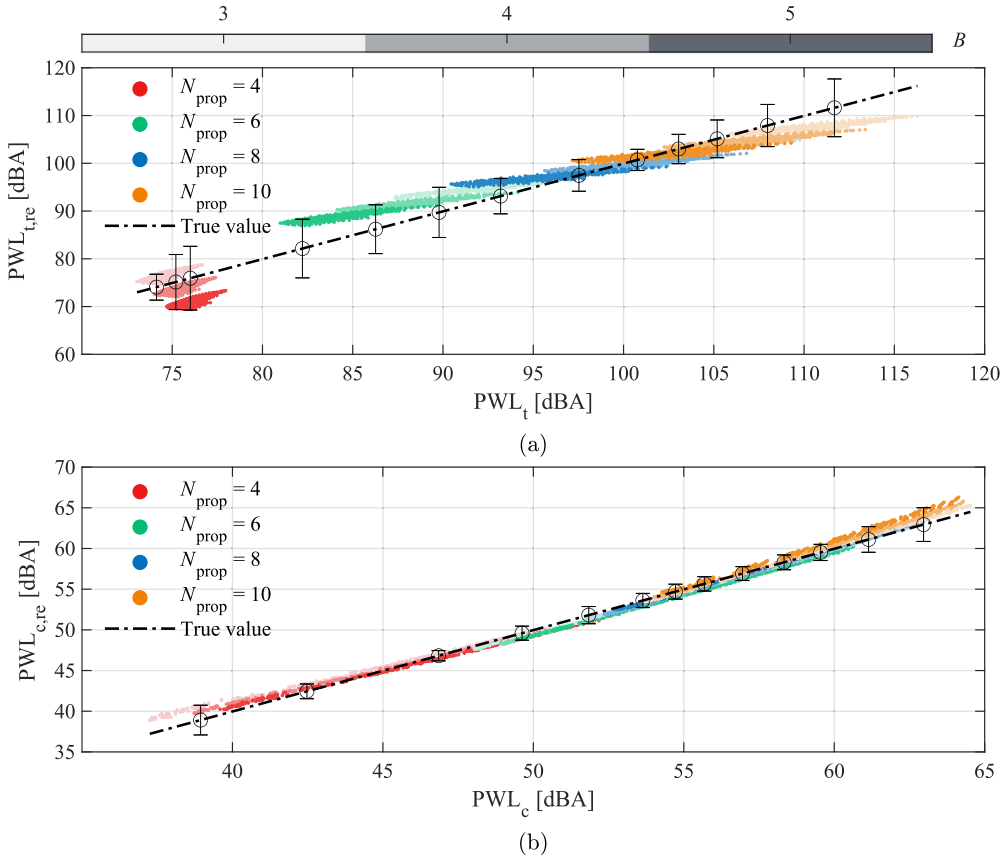


**Fig. 11.** Comparisons between PWLs obtained using fitting coefficients and design tool for (a) takeoff and (b) cruise stages. The results corresponding to $N_{prop}$ = 4, 6, 8, and 10 are illustrated in red, green, blue, and yellow, respectively. Decreasing $B$ from 5 to 3 is depicted by reducing the shades of colour. The 'true values' obtained using the low-fidelity design tool are presented in the dash-dot line. Error bars are noted, illustrating the maximum deviation between the $PWL_{re}$ and true values at the corresponding PWLs.

**Table 7**
Summary of the computed values of fitting coefficients and the corresponding ranges during takeoff and cruise.

| | | $K_P$ | $K_D$ | $K_B$ | C |
|---|---|---|---|---|---|
| Takeoff | Value | 3.2 | -20.3 | -2.9 | 124.1 |
| | Range | 1.8 to 4.7 | -46.0 to 17.1 | -4.8 to -0.8 | 117.6 to 130.8 |
| Cruise | Value | 0.0 | 14.1 | 0.5 | 102.2 |
| | Range | -0.5 to 0.2 | -2.2 to 16.7 | -0.2 to 0.7 | 100.0 to 103.2 |

In addition to the fitting values shown in Equation (13) and (14), a possible range of deviation for each coefficient exists. The ranges are evaluated as the maximum differences between the recovered PWLs and those computed using low-fidelity design framework, achieved by holding the other coefficients constant. For instance, the range of $K_P$ for takeoff is determined by

$$K_P = \frac{\mathrm{PWL_t} + 20.3\log_{10}D - 60\log_{10}M_t + 2.9B - 10\log_{10}N_{prop} - 124.1}{\log_{10}P_s}. \tag{15}$$

A summary of the computed values and ranges for each fitting coefficient is presented in Table 7. The computed coefficients generally match the mean of the possible values. The precision of most coefficients is high with the exception of $K_D$, attributing to its substantial magnitude when compared to other computed coefficients.

The quality of the regression model is demonstrated by plotting the recovered PWLs for takeoff and cruise against those obtained from the low-fidelity design framework ('true values') in Fig. 11 (a) and (b), respectively. The PWLs linked to $N_{prop}$ = 4, 6, 8, and 10 are presented using red, greed, blue, and yellow colours, respectively. A decrease in $B$ is reflected by reducing the shades of colour. The true values of PWL are depicted along a dash-dot line, with annotated error bars representing the maximum deviation of recovered PWLs with respect to the true values. Fig. 11 shows that Equation (13) and (14) can predict the PWLs of the vehicle reasonably well for both takeoff and cruise stages. The maximum error in $PWL_{re}$ are 6.7 dBA for takeoff and 1.1 dBA for cruise.

An important aspect of the regression model is that it allows for the assessment of design parameters on the emitted noise. For the takeoff stage, $M_t$ is shown to have the largest coefficient when comparing to other powertrain inputs, indicating that takeoff noise is highly sensitive to changes in $M_t$. Increasing $M_t$ is found to elevate the tonal component of $PWL_{t,re}$, aligning with the results of Akiwate et al. [54], who demonstrated that increasing $M_t$ and holding $s$ constant can largely enhance the tonal noise. Propeller diameter $D$ is shown to be the next sensitive contributor to takeoff noise, followed by $N_{prop}$ and $P_s$. The signs of $K_D$ and $K_N$ indicate that using larger and fewer propellers helps reducing $PWL_{t,re}$, while increasing shaft power leads to greater noise. This observation is consistent with the discussion presented in Section 3.1. Next, $K_B$ is observed to have a comparable magnitude to its counterpart in Equation (11), and increasing $B$ reduces $PWL_{t,re}$. This result may be attributed to the balance between tonal and broadband noise, as increasing $B$ while keeping $s$ constant significantly reduces the prominence of tonal noise [54]. The A-weighting process may further attenuate the tonal component, contributing to decreasing the overall $PWL_{t,re}$.

For the cruise stage, some fitting coefficients vary significantly from those identified for takeoff, suggesting a shift in the role of powertrain parameters as operating conditions change [54,55]. The tip Mach number remains the most influential parameter in terms of noise emission and is proportional to $PWL_{c,re}$. The magnitudes of $K_D$ and $K_N$ indicate

that both the size and number of propeller have notable influence in modulating the noise level during cruise. In contrast to Equation (13), increasing both $D$ and $N_{\text{prop}}$ is seen to elevate noise. The observation is likely due to the intertwined relation between design choices. The magnitude of $K_P$ in Equation (14) drops to zero, which can be attributed to the major role of takeoff on the determination of the installed power. Compared to takeoff, the required power during cruise is less significant. Additionally, the contribution from broadband sources, which correlates more strongly with the tip Mach number, is expected to increase relative to the tonal sources. The positive sign of $K_B$ suggests that increasing $B$ will elevate the overall $\text{PWL}_{\text{c,re}}$, which is opposite to that observed in Equation (11) and (13). This discrepancy is related to the larger contribution of broadband sources of noise. Nevertheless, the small magnitude of $K_B$ indicates that varying $B$ does not significantly impact $\text{PWL}_{\text{c,re}}$. This is likely due to the reduced contribution of tonal noise in overall PWL, as propellers operate at lower RPMs compared to during takeoff [54,19]. The discrepancies in fitting coefficients between Equation (14) and (13) can also be attributed to the influence of A-weighting, as the tonal harmonics are at much lower frequencies during cruise than during takeoff.

To further elucidate the relation between vehicle design and noise emission, the equations for estimating PWLs are reformulated into terms associated with vehicle attributes, such as maximum takeoff weight $W_{\text{MTOM}}$ and total rotor disk area $A_{\text{disk}}$. For the takeoff noise, this is achieved by substituting Equations (1) and (6) into Equation (13), where $P_{\text{s}}$ and $M_{\text{t}}$ can be expressed through common terms of $W_{\text{MTOM}}$ and $D$ as shown below

$$P_{\text{s}} = \frac{1}{\text{FM}}\sqrt{\frac{2T^3}{\rho\pi D^2}}, \text{and} \tag{16}$$

$$M_{\text{t}} = \frac{2}{c_o D}\sqrt{\frac{6T}{\rho s\pi C_L}}. \tag{17}$$

Note that $T$ is the thrust produced per propeller and is given by

$$T = \frac{W_{\text{MTOM}}}{N_{\text{prop}}}. \tag{18}$$

After rearranging the terms and considering the total propeller disk area $A_{\text{disk}} = N_{\text{prop}}\frac{\pi}{4}D^2$, we arrive at

$$\begin{aligned}\text{PWL}_{\text{t,re}} = {} & \underbrace{\frac{1}{2}K_P\log_{10}\left(\frac{\pi^2}{32\rho\text{FM}^2}\right) + 30\log_{10}\left(\frac{24}{c^2\rho s\pi C_L}\right) + 20\log_{10}\frac{\pi}{4} + \text{C}}_{\text{term 1}} \\ & + \underbrace{\left(\frac{3}{2}K_P + 30\right)\log_{10} W_{\text{MTOM}}}_{\text{term 2}} - \underbrace{\left(\frac{3}{2}K_P + 20\right)\log_{10} A_{\text{disk}}}_{\text{term 3}} \\ & + \underbrace{(K_D + 2K_P - 20)\log_{10} D}_{\text{term 4}} + \underbrace{K_B B}_{\text{term 5}}\end{aligned} \tag{19}$$

Term 1 from Equation (19) represents a group of constants that stem from the assumptions made in this study. Terms 2, 3, 4, and 5 represent contributions of $W_{\text{MTOM}}$, $D$, $A_{\text{disk}}$, and $B$ towards the $\text{PWL}_{\text{t,re}}$, respectively. Using the values of fitting coefficients for takeoff, the final form of Equation (19) is determined to be

$$\begin{aligned}\text{PWL}_{\text{t,re}} = {} & 5.8 + 34.8\log_{10} W_{\text{MTOM}} - 24.8\log_{10} A_{\text{disk}} \\ & - 33.9\log_{10} D - 2.9B,\end{aligned} \tag{20}$$

Following the same approach, Equation (14) can be expressed as

$$\begin{aligned}\text{PWL}_{\text{c,re}} = {} & -15.2 + 30\log_{10}\frac{W_{\text{MTOM}}}{r_{LD}} - 20\log_{10} A_{\text{disk}} \\ & - 5.9\log_{10} D + 0.5B,\end{aligned} \tag{21}$$

where cruise $T$ is replaced by $\frac{W_{\text{MTOM}}}{r_{LD}}$, with $r_{LD}$ representing the lift-to-drag ratio of the vehicle.

These equations allow for a direct comparison of vehicles with the same weight and total disk area, i.e., the same disk loading. As shown in Equation (20) and (21), PWLs in both takeoff and cruise are sensitive to changes in $W_{\text{MTOM}}$ due to the substantial magnitude of its coefficient. As expected, increasing $W_{\text{MTOM}}$ increases PWL in both takeoff and cruise since the required thrust to lift the vehicle and sustain level flight is proportional to the vehicle weight. In addition to $W_{\text{MTOM}}$, the total disk area is found to be a notable contributor to $\text{PWL}_{\text{t,re}}$ and $\text{PWL}_{\text{c,re}}$. It is observed that increasing $A_{\text{disk}}$ and $D$ leads to noise reduction. This benefit arises from an enhanced propulsion system efficiency that requires a smaller RPM, consequently reducing the tonal noise. Furthermore, the influence of $D$ on noise reduction is more pronounced during takeoff than cruise. When disk loading is held constant, the results indicate a trend where a tilt-rotor vehicle with fewer but larger diameter propellers is preferable to one with a large number of smaller rotors. This preference is primarily due to the lower rotational speeds of large propellers, coupled with human perception that is less sensitive to low BPFs. These findings are consistent with the observations from Figs. 3 and 4 from Section 3.1.

## 4. Conclusion

In this investigation, a design exploration of the electric vertical takeoff and landing (eVTOL) vehicle was performed for a 2050 time horizon using a low-fidelity design framework developed at Delft University of Technology. The vehicle architecture employed here was chosen as a tilt-rotor combined with a conventional airframe, a design choice aimed at fulfilling the mission requirements of both Urban Air Mobility (UAM) and Regional Air Mobility (RAM) operations. The vehicle was designed to operate with a single pilot and can carry four passengers. A set of Top-Level Aircraft Requirements (TLARs) were considered as design variables in this investigation. These TLARs were identified as operating range $R$, speed $V$, number of propellers $N_{\text{prop}}$, and wing area $S$. The variables were altered to facilitate a systematic exploration of various conceptual designs, thereby providing a comprehensive analysis of the potential performance and capabilities of the eVTOL vehicle. The influence of these design variables were evaluated from the perspectives of energy consumption, noise emission, and commercial viability.

Based on the assessment on $N_{\text{prop}}$ and $S$, it is found that the tilt-rotor vehicle with wing is deemed inadequate to operate at low speed of 100 km/h regardless of the configuration. The wings cannot generate sufficient lift to sustain level flight for most of the investigated $R$. At higher speeds, a small $S$ coupled with large $N_{\text{prop}}$ is favoured in terms of energy consumption per pax-km and operating expenses per pax-km. Concerning the noise emission, the design preference on $N_{\text{prop}}$ flips for both takeoff and cruise stages. Following the evaluation of $N_{\text{prop}}$ and $S$, the investigation also assesses performance variables with respect to energy consumption, noise level, and operating expenses. For the purpose of conserving energy, low-speed operation is preferred, with the minimum $\text{EC}_{\text{pk}}$ is found to be approximately 0.1 kWh/pax/km. The minimum $\text{PWL}_{\text{t}}$ is mostly observed in low-speed or short-range operations and is approximately 75 dBA, while the ideal $\text{PWL}_{\text{c}}$ is generally seen to increase with rising $V$, featuring a minimal value around 40 dBA, regardless of $R$. To offer some guidance on business planning for tilt-rotor vehicles, the ideal $\text{OE}_{\text{pk}}$ is evaluated across different $V$ and $R$. The commercial competitive operations are found to be those featuring shorter flight hours, as the dominating personnel cost are low. In contrast, the energy efficient operations favour low speed but greater than 100 km/h since less energy is consumed during cruising. Furthermore, a sensitivity study of noise emissions with respect to key powertrain pa-

rameters is carried out. With basic information such as the shaft power, propeller diameter, tip Mach number, number of blades, and number of propellers, the A-weighted sound power level during takeoff and cruise can be quickly estimated through a regression model. In consistent with the evaluation on $N_{prop}$, the model suggests that a design featuring a few large propellers is preferred for lower noise emissions, contrasting with the design preference for low energy consumption and costs, which favours a greater number of smaller propellers.

In summary, several intriguing findings have emerged from this design exploration. For operations characterized by low operating speed and short operating range, a design that employs a multicopter architecture is more suitable. For operations that demand long-range capabilities, achieving a higher cruise speed is pivotal to counter the increase in battery weight. The critical speed falls in between 125 km/h and 175 km/h, where the reliance on propeller for lift support gradually perishes across investigated operating ranges. The most commercially competitive operating conditions do not align with the most energy-efficient ones, as the energy-related cost is found to be insignificant compared to personnel cost. Commercially viable operations feature a large number of propellers, which provides little advantage in reducing energy-related cost but significantly increases the emitted noise. Hence, a smaller number of propeller is preferred concerning the social community acceptance. The study demonstrates the necessity for multidisciplinary vehicle optimization for urban air mobility operations, as different ideal designs are produced based on the environmental, societal, and economic constraints applicable. The priority of optimization can vary depending on the mission objective and business plan.

## CRediT authorship contribution statement

**Sen Wang:** Writing – review & editing, Writing – original draft, Visualization, Methodology, Investigation, Data curation. **Lourenço Tércio Lima Pereira:** Writing – review & editing, Supervision, Software, Methodology, Conceptualization. **Daniele Ragni:** Writing – review & editing, Supervision, Funding acquisition, Conceptualization.

## Declaration of competing interest

The authors declare that they have no known competing financial interests or personal relationships that could have appeared to influence the work reported in this paper.

## Acknowledgement

The research presented in this paper has been performed in the framework of the COLOSSUS project (Collaborative System of Systems Exploration of Aviation Products, Services and Business Models) and has received funding from the European Union Horizon Europe program under grant agreement No. 101097120. Views and opinions expressed are however those of the authors only and do not necessarily reflect those of the European Union or CINEA. Neither the European Union nor the granting authority can be held responsible for them. The authors would like to thank Marco Fioriti, Marco Borghi, and Guido Pavan from Politecnico di Torino; Vincenzo Cusati and Manuela Ruocco from SmartUp Engineering srl; as well as Michele Tuccillo and Fabrizio Nicolosi from the University of Naples Federico II for their assistance and development of the cost model. During the preparation of this work the author(s) used ChatGPT to assist with grammar revisions. After using it, the author(s) reviewed and edited the content as needed and take(s) full responsibility for the content of the publication.

## Data availability

Data will be made available on request.

## References

[1] A. Straubinger, R. Rothfeld, M. Shamiyeh, K.-D. Büchter, J. Kaiser, K.O. Plötner, An overview of current research and developments in urban air mobility–setting the scene for uam introduction, J. Air Transp. Manag. 87 (2020) 101852.
[2] U.A.M. FAA, Concept of Operations V1. 0, US Department of Transportation Federal Aviation Administration, Washington DC, 2020.
[3] M.D. Moore, Concept of operations for highly autonomous electric zip aviation, in: 12th AIAA Aviation Technology, Integration, and Operations (ATIO) Conference, 2012, pp. 1–15.
[4] G. Palaia, K. Abu Salem, V. Cipolla, V. Binante, D. Zanetti, A conceptual design methodology for e-vtol aircraft for urban air mobility, Appl. Sci. 11 (22) (2021) 10815.
[5] J.M. Vegh, E. Botero, M. Clark, J. Smart, J.J. Alonso, Current capabilities and challenges of ndarc and suave for evtol aircraft design and analysis, in: 2019 AIAA/IEEE Electric Aircraft Technologies Symposium (EATS), IEEE, 2019, pp. 1–19.
[6] A. Manthiram, Y. Fu, Y.-S. Su, Challenges and prospects of lithium–sulfur batteries, Acc. Chem. Res. 46 (5) (2013) 1125–1134.
[7] L.A. Garrow, B.J. German, C.E. Leonard, Urban air mobility: a comprehensive review and comparative analysis with autonomous and electric ground transportation for informing future research, Transp. Res., Part C, Emerg. Technol. 132 (2021) 103377.
[8] E.J. Berg, C. Villevieille, D. Streich, S. Trabesinger, P. Novák, Rechargeable batteries: grasping for the limits of chemistry, J. Electrochem. Soc. 162 (14) (2015) A2468.
[9] T. Kim, W. Song, D.-Y. Son, L.K. Ono, Y. Qi, Lithium-ion batteries: outlook on present, future, and hybridized technologies, J. Mater. Chem. A 7 (7) (2019) 2942–2964.
[10] C.L. Pastra, C. Hall, G. Cinar, J. Gladin, D.N. Mavris, Specific power and efficiency projections of electric machines and circuit protection exploration for aircraft applications, in: 2022 IEEE Transportation Electrification Conference & Expo (ITEC), IEEE, 2022, pp. 766–771.
[11] W. Ng, A. Datta, Hydrogen fuel cells and batteries for electric-vertical takeoff and landing aircraft, J. Aircr. 56 (5) (2019) 1765–1782.
[12] P. Nathen, A. Strohmayer, R. Miller, S. Grimshaw, J. Taylor, Architectural performance assessment of an electric vertical take-off and landing (e-vtol) aircraft based on a ducted vectored thrust concept, Tech. Rep., Lilium GmbH, Claude-Dornier StraeSSe, Weßling, Germany, 2021.
[13] N. EASA, Study on the societal acceptance of urban air mobility in Europe, 2021.
[14] S.A. Rizzi, D.L. Huff, D.D. Boyd, P. Bent, B.S. Henderson, K.A. Pascioni, D.C. Sargent, D.L. Josephson, M. Marsan, H.B. He, et al., Urban air mobility noise: Current practice, gaps, and recommendations, Tech. Rep., NASA, 2020.
[15] L. Babetto, A. Kirste, J. Deng, M. Husemann, E. Stumpf, Adoption of the urban air mobility system: analysis of technical, legal and social aspects from a European perspective, J. Air Transp. Res. Soc. 1 (1) (2023) 152–174.
[16] P.S. Prakasha, N. Naeem, K. Amadori, G. Donelli, J. Akbari, F. Nicolosi, L.K. Franzén, M. Ruocco, T. Lefebvre, B. Nagel, Colossus EU project – collaborative sos exploration of aviation products, services and business models: overview and approach, in: 34th ICAS Congress, 2024.
[17] M. Spieck, L.K. Franzén, K. Amadori, P.S. Prakasha, N. Naeem, A capability-focused approach to model complex, multi-layered systems-of-systems, in: AIAA Aviation Forum and Ascend 2024, 2024, p. 3559.
[18] A. Straubinger, F. Helmchen, K.O. Ploetner, J. Kaiser, Proposing a scenario-based estimation of global urban air mobility demand, in: Aiaa Aviation 2021 Forum, 2021, p. 3207.
[19] L.T. Lima Pereira, S. Wang, D. Ragni, A preliminary design framework for performance and noise assessment of urban air mobility vehicles, in: 30th AIAA/CEAS Aeroacoustics Conference (2024), 2024, p. 3334.
[20] N. Peteilh, T. Klein, T.Y. Druot, N. Bartoli, R.P. Liem, Challenging top level aircraft requirements based on operations analysis and data-driven models, application to takeoff performance design requirements, in: AIAA Aviation 2020 Forum, 2020, p. 3171.
[21] J. Leigh, National campaign development test executive summary, Tech. Rep., NASA, 2023.
[22] P. Shiva Prakasha, N. Naeem, P. Ratei, B. Nagel, Aircraft architecture and fleet assessment framework for urban air mobility using a system of systems approach, Aerosp. Sci. Technol. 125 (2022) 107072, SI: DICUAM 2021.
[23] A. Betz, Introduction to the Theory of Flow Machines, Elsevier, 2014.
[24] J. Roskam, Airplane Design: Component Weight Estimation, Roskam Aviation and Engineering Corporation, 1985.
[25] J.A. Cole, L. Rajauski, A. Loughran, A. Karpowicz, S. Salinger, Configuration study of electric helicopters for urban air mobility, Aerospace 8 (2) (2021) 54.
[26] M. Drela, M.B. Giles, Viscous-inviscid analysis of transonic and low Reynolds number airfoils, AIAA J. 25 (10) (1987) 1347–1355.
[27] J. Katz, A. Plotkin, Low-Speed Aerodynamics, vol. 13, Cambridge University Press, 2001.
[28] D.B. Hanson, Near-field frequency-domain theory for propeller noise, AIAA J. 23 (4) (1985) 499–504.
[29] R. Schlinker, R. Amiet, Helicopter rotor trailing edge noise, in: 7th Aeroacoustics Conference, 1981, p. 2001.
[30] B. Magliozzi, D. Hanson, R. Amiet, Propeller and propfan noise, in: Aeroacoustics of Flight Vehicles: Theory and Practice, vol. 1, 1991, pp. 1–64.

[31] F.d. Monteiro, D. Ragni, F. Avallone, T. Sinnige, Low-order acoustic prediction tool for estimating noise emissions from distributed propeller configurations, in: AIAA AVIATION 2023 Forum, 2023, p. 4180.
[32] F. De Prenter, A. Zarri, D. Casalino, Low-cost computational modeling of aeroacoustic interactions between adjacent propellers, in: 30th AIAA/CEAS Aeroacoustics Conference (2024), 2024, p. 3069.
[33] Y. Fuerkaiti, D. Casalino, F. Avallone, D. Ragni, Aircraft community noise prediction in 3d environment using Gaussian beam tracing, in: 28th AIAA/CEAS Aeroacoustics 2022 Conference, 2022, p. 3079.
[34] N.U.A. Mobility, Urban air mobility (uam) market study, Retrieved the 30 (2018) 2019.
[35] D. Raymer, Aircraft Design: a Conceptual Approach, American Institute of Aeronautics and Astronautics, Inc., 2012.
[36] A. Cooke, E. Fitzpatrick, Helicopter Test and Evaluation, John Wiley & Sons, 2009.
[37] H. Fletcher, W.A. Munson, Loudness, its definition, measurement and calculation, Bell Syst. Tech. J. 12 (4) (1933) 377–430.
[38] A. Brown, W.L. Harris, Vehicle design and optimization model for urban air mobility, J. Aircr. 57 (6) (2020) 1003–1013.
[39] G. Van Kuik, The Fluid Dynamic Basis for Actuator Disc and Rotor Theories, revised second edition, IOS Press, 2022.
[40] N. Rosenberger, P. Rosner, P. Bilfinger, J. Schöberl, O. Teichert, J. Schneider, K. Abo Gamra, C. Allgäuer, B. Dietermann, M. Schreiber, et al., Quantifying the state of the art of electric powertrains in battery electric vehicles: comprehensive analysis of the tesla model 3 on the vehicle level, World Electr. Veh. J. 15 (6) (2024) 268.
[41] K. White, A.W. Bronkhorst, M. Meeter, Annoyance by transportation noise: the effects of source identity and tonal components, J. Acoust. Soc. Am. 141 (5) (2017) 3137–3144.
[42] M. Fioriti, V. Vercella, N. Viola, Cost-estimating model for aircraft maintenance, J. Aircr. 55 (4) (2018) 1564–1575.
[43] M. Fioriti, V. Vercella, et al., A parametric cost model for estimating civil aircraft line and base maintenance, Int. Rev. Aerosp. Eng. 12 (6) (2019) 250–260.
[44] V. Vercella, M. Fioriti, N. Viola, Towards a methodology for new technologies assessment in aircraft operating cost, Proc. Inst. Mech. Eng., G J. Aerosp. Eng. 235 (8) (2021) 879–892.
[45] M.D. Maisel, The History of the XV-15 Tilt Rotor Research Aircraft: from Concept to Flight, vol. 17, National Aeronautics and Space Administration, Office of Policy and Plans . . . , 2000.
[46] W. Johnson, Rotorcraft Aeromechanics, vol. 36, Cambridge University Press, 2013.
[47] G.J. Ruijgrok, Elements of Aviation Acoustics, Delft University Press, 1993.
[48] G. Ruijgrok, F. van Deventer, External Noise of Light Propeller-Driven Aircraft, Delft University of Technology, Department of Aerospace Engineering, Delft, the Netherlands, 1976.
[49] Anon, Prediction procedure for near-field and far-field propeller noise, Tech. Rep., SAE, 1977.
[50] S. Glegg, W. Devenport, Aeroacoustics of Low Mach Number Flows: Fundamentals, Analysis, and Measurement, Academic Press, 2017.
[51] D. Hanson, Propeller noise caused by blade tip radial forces, in: 10th Aeroacoustics Conference, 1986, p. 1892.
[52] H.H. Hubbard, Aeroacoustics of Flight Vehicles: Theory and Practice, vol. 1, National Aeronautics and Space Administration, Office of Management . . . , 1991.
[53] D. Kurtz, J. Marte, A review of aerodynamic noise from propellers, rotors, and lift fans, Tech. Rep., NASA, 1970.
[54] D.C. Akiwate, A.B. Parry, P. Joseph, C.C. Paruchuri, On the balance between the tonal and broadband noise of uninstalled propellers, in: AIAA AVIATION 2021 FORUM, 2021, p. 2308.
[55] K. Baskaran, N.S. Jamaluddin, A. Celik, D. Rezgui, M. Azarpeyvand, Effects of number of blades on propeller noise, J. Sound Vib. 572 (2024) 118176.